DOI: 10.17725/rensit.2023.15.263

A Neoteric View of sp^2 Amorphous Carbon

Elena F. Sheka

Peoples' Friendship University of Russia, https://www.rudn.ru/
Moscow 117198, Russian Federation
E-mail: sheka@icp.ac.ru

Received March 26, 2023, peer-reviewed April 03, 2023, accepted April 10. 2023

Abstract: **Presented is a concentrated synopsis of facilities of empirical and virtual analytics that, once applied, have provided a fully new vision of sp^2 amorphous carbons. This study proved that the solids are multilevel structures, started with the first-level basic structural units (BSUs) and accomplished as macroscopic agglomerates of globular structures, consisting, in its turn, of stacked BSUs. BSUs present necklaced graphene molecules, size, and shape of which are governed by the relevant graphene domains while chemical composition in addition to basic carbon is controlled with heteroatoms of the necklaces. This study shows that BSUs and stacks of BSUs determine the short-range order of the solids and are the main subject of the applied analytics. The synopsis consists of two parts related to empirical and virtual analytics. The former is composed of sections related to structural determination, total and atomic chemical content evaluation and elicitation of the covalent bond composition. The second presents new analytic approaches based on the Digital Twins concept and virtual vibrational spectrometry. The synopsis is configured as an atlas composed of generalized pictures accompanied with necessary explanations to be discussed in detail in the extended references.**

Keywords: **sp^2 amorphous carbons; molecular short-range order; necklaced graphene molecules; structural and compositional analytics; virtual spectrometry analytics**

UDC 004.942, 547.022.1

Acknowledgments: The author is thankful to colleagues, without collaboration with whom this atlas presentation would not be possible. My deep gratitude to I. Natkaniec, N.N. Rozhkova, Ye.A. Golubev, the late B.S. Rasbirin, Ye.N. Kabachkov, Ye.U. Ipatova, the late K. Holderna-Natkaniec, K. Druzhbicky, Y.M. Shul'ga, V.M. Mel'nikov, D.K. Nelson, A.N. Starukhin, V. Tkachev. M.F. Budyka. I greatly appreciate fruitful discussions with M.L. Terranova, S.P. Gubin, and A.Tadger. My invaluable gratitude to N.A. Popova, V.A. Popova for assistance with calculations and results treatment. This paper has been supported by the RUDN University Strategic Academic Leadership Program.

For citation: Elena F. Sheka. A Neoteric View of sp^2 Amorphous Carbon. *RENSIT: Radioelectronics. Nanosystems. Information Technologies,* 2023, 15(3):263-294e. DOI: 10.17725/rensit.2023.15.263.

Content

1. A CONCISE HISTORICAL INTRODUCTION

The last two decades have seen a profound breakthrough in our understanding of sp^2 amorphous carbon (aC). First, this was due to the epoch-making development of graphenics – a new material science. The new scientific trend revived a huge interest in solid carbon in general, and gave rise to the first, and then subsequently more convincing guesses that the history of graphenics did not begin in 2010 but goes back centuries ago, and that it is precisely aC that shows the way. The second important circumstance, which stimulated a new interest in amorphous carbon, is the highly elevated level of research into the structure and chemical composition of materials. In the rays of these two illuminations, sp^2 aC began to play with completely new facets. The purpose of this review is to introduce readers to a new vision of this old material.

My first personal encounter with sp^2 aC was in 2005. Being engaged in fullerenes at that time, I was puzzled by the search for evidence of the presence of this sp^2 nanocarbon in nature. Having heard about its possible observation in a natural mineral called shungite carbon, huge deposits of which are located within Russian Karelia, I went to sort it out on the spot. Scholars from the Institute of Geology of the Karelian Scientific Center of the Russian Academy of Sciences, who worked on these deposits, told me many interesting things about this mineral, but its connection with fullerenes has not been confirmed. However, fairy tale-like stories about its outstanding properties, its belonging to the family of nanoscale solid carbons, and the high degree of carbonization reaching more than 98%, did not allow for forgetting this amazing substance. Throughout the formation and further development of the radical concept of sp^2 nanocarbons, which then included fullerenes, carbon nanotubes, and first new graphene materials, such as graphene oxide and reduced graphene oxide (rGO), my attention again and again turned to shungite carbon. After a deep analysis in collaboration with N.N. Rozhkova it was suggested that the mineral is of a complex multilevel structure based on molecular-like compositions, which are nanosize graphene domains framed along the perimeter by heteroatoms that provide complete and/or partial termination of dangling valence bonds of the domain edge atoms [1]. This assumption was in line with fundamentals of chemical processes in nanoscale systems presented in a conceptual article by R. Hofmann, Nobel Prize winner in chemistry [2]. Thus, the idea arose that the basic structural unit (BSU) of shungite carbon is a necklaced graphene molecule (NGM). Analyzing the available chemical content data, we assumed that hydrogen and oxygen are the main components of this BSU's heteroatom necklace.

At the same time, all geophysicists share common opinion that shungite carbon belongs to amorphous solids, i.e., is a member of the aC family. In turn, this body belongs to covalent solids, in which the short-range order [3] is evidently determined by a particular configuration of covalent sp^2 C–C bonds. Chemistry teaches us that covalent bonds are extremely persistent, are characterized with a well-defined local topology, and tend to strongly resist changing their lengths and angles to ensure a stable chemical composition of substances. Therefore, it seems reasonable to assume that, within the limits of the short-range order space, sp^2 C–C bonds retain their standard topology, thereby separating the graphene domain limited in size from the total massif of an extended honeycomb structure. A further variation in the domain arrangement ensures the disorder of the solid. In this sense, shungite carbon is analogous to covalent molecular amorphics, in which the short-range order is determined with the basic standard molecules [4]. Accordingly, it is natural to assume that the NGMs, suggested to explain the structure of shungite carbon, can be considered as BSUs of sp^2 aC of any origin. Moreover, the well-studied multilevel structure of shungite carbon can be taken as the basis for all aCs of this type.

The first bridge, uniting shungite carbon with other sp^2 aCs was built when comparing vibrational spectra of shungite carbon and one of the synthetic rGOs [5]. It would seem that there was nothing to prevent the idea of NGMs as BSUs from being a fundamental concept for the entire

class of sp^2 aCs. However, one day, on the desk of one of my colleagues, I saw two flasks filled with black powder, with manufacturer's labels pasted on, saying "C 100%", and with CB624 and CB632 inscriptions indicating SIGMA-ALDRICH MERCK as producers. Both products were synthetic sp^2 aC known as black carbon [6]. The indisputable authority of the manufacturer and the high price of the products did not leave a shadow of doubt about its quality, and none of my arguments based on the quantum nature of the matter and asserting the impossibility of the existence of C 100% nanoscale graphene domains were heard. The only way to solve the problem of the 100% nature of the carbons was to conduct a thorough study of a set of sp^2 aC using as many available analytical methods as possible. Seven samples listed in **Table 1** were selected. All of them were of the maximum carbonization [7-12]. The first three are natural sp^2 aCs, the next two are synthetic technical graphenes – rGOs [13] obtained in various ways, and the last two are the above-mentioned black carbons from the SAM. All samples were analyzed by the same set of methods under equal conditions. Three groups of analytic techniques were used: 1) structural one, 2) evaluating the overall atomic composition of the samples, and 3) determining the atomic composition of covalent C–A bonds (A = C, H, O).

The results obtained allowed us to solve the main problem and obtain indisputable evidence that BSUs of sp^2 aCs have a unified nature and are NGMs, the size of whose domains and atomic composition of the relevant necklaces are determined by the chemical history of the amorphics' origin. The next result showed that all the studied aCs have a multilevel structure based on zero-level BSUs with subsequent aggregation of the units into stacks, globules, and micro- and/or macroscopic agglomerates of higher levels. The third result is that, due to the structural and compositional complexity of sp^2 aCs, analytical testing of samples cannot be single-technique and requires the use of a set of methods. Last, when the multi-technique analytics of sp^2 aCs is mastered, quantum–chemical modeling of the structure, composition, and properties of their BSUs becomes possible. Thus obtained model BSUs open the way to new analytics of the sp^2 aCs that is a virtual one and is based on the Digital Twins concept [14].

The current review presents a consolidated view on these multi-technique analytics applied to a representative set of sp^2 aCs. Since discussed results are too numerous, an atlas-like format was chosen to facilitate the presentation. Although the results, obtained with the participation of the author, make the main contribution to the figures and tables presented below, those obtained in other groups were also taken into account when compiling the review. Nevertheless, the author apologizes in advance for the possible omission of other important results unknown to her and expresses her gratitude for the relevant indications.

2. GENERAL CHARACTERISTICS OF THE CARBON AMORPHICITY

As mentioned earlier, sp^2 aCs present only a part of aCs that form a large allotropic class of solids, both natural and synthetic. Many books and reviews are devoted to the issue, among which [15–31], but a few, allow the reader to create his/her own idea of the complexity and high science intensity of the touched issue. Natural amorphics are products of nature's laboratory for geological billion-million-year time. Geologists' examinations suggest a few classification schemes of carbon species [32–35]. One of which, presenting a continuous evolution of aC as increasing

Table 1

sp^2 Amorphous carbons selected for a joint study

No	Samples	Abbreviation	Origin	References
1	Shungite carbon	ShC	Shun'ga deposit of Karelia, Russia	[7]
2	Anthraxolite	AnthX	Pavlovsk deposit of Novaya Zemlya, Russia	[8]
3	Anthracite	AnthC	Donetsk deposit, Russia	[9]
4	rGO	Ak–rGO	Institute of the Inorganic Chemistry, RAS, Moscow, Russia	[10]
5	rGO	TE–rGO	Institute of the Chemical Physics, RAS, Moscow, Russia	[11]
6	Black carbon	CB632	Sigma-Aldririch-Merk company, USA	[12]
7	Black carbon	CB624	Sigma-Aldririch-Merk company, USA	[12]

carbonization rank of pristine carbonaceous masses into ordered crystalline graphite thus exhibiting the main stream of carbon life in nature [36], is shown in **Fig 1***a*. As seen in the figure, a general motion is split into two gloves, the left of which starts with plants and sediments, proceeds through sapropels to brown coals, and later to convenient coals and anthracite, finishing with graphite. As for the right glove, it covers carbonization of pristine gas and distillate oil and proceeds through petroleum and naphthoids, to asphalts, and then to kerites, anthraxolites, and shungites. As in the previous case, graphite is the endpoint. This scheme is related to sp^2 aC that actually dominates in nature [36]. Natural sp^3 aC is not as largely distributed, due to which diamond-like amorphous solids have only recently become top issues of the carbon mineralogy [37,38].

The family of synthetic aCs is quite large, covering species different not only by the carbonization rank, but also by a mixture of sp^2 and sp^3 components. Analogously to natural species, synthetic amorphics were classified as well [36,39,40] and the relevant classification scheme is presented in Fig. 1*b*. Previously ternary, it was completed to a rhombic one to take into account oxygen as another important ingredient [36]. Comparing schemes presented for natural and synthetic aCs, it becomes evident that if natural aCs belong to sp^2 carbon family and are carbonization-rank characterized, synthetic aCs are mainly sp^3-configured solid carbons. The sp^2 group

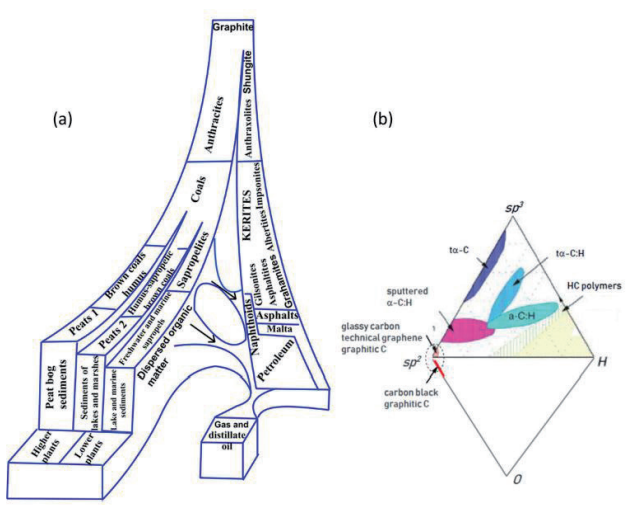

Fig. 1. *General classification of amorphous carbon. (a) Carbon life path in nature according to the Uspenskiy's classification. (b) Rhombic diagram of synthetic amorphous carbon-hydrogen-oxygen system.*

of the synthetic species, characterized by the highest carbonization, takes only a small oval-mapped place. Because of the small amount of sp^3 solid aC in nature, special technologies to produce ta–C, ta–CH (t means tetragonal), and sputtered sp^2 & sp^3 mixed a–C:H products were developed. It is necessary to complement this part of carbon solids by graphite oxide (GO), which corresponds to sp3 configured carbon with up to ~ 40% of oxygen in the case of complete oxygenation. As for sp^2 synthetic aCs, for a long time they were presented by multi-tonnage industrial production of glassy carbon, covering graphitic, black, activated, and other highly carbonized products [41]. However, the graphene era called to life a new high-tech material—technical graphenes, or rGOs [13], which are the final product of either oxidation-reduction [10,42] or oxidation-thermally-shocked exfoliation [11,43] of nanosize graphite. Two new members of this community are on the way—laser-induced graphene (LIG) manufactured by multiple lasing on cloth, paper, and food [44] and extreme quality flash graphene (FG) [45], closest in ordering to graphite.

Despite aCs having been the object of study and practical use for hundreds of years, only recently have they been considered from the general concept of the solid-state physics [36] basing on fundamentals of the amorphicity of solids accumulated in monographs [3]. The first conceptual issue concerns a considerable degree of amorphous solid ordering that is subdivided into short-range (local) and medium-range ones, the boundary between which passes around a few nm. The second issue is related to the direct interconnection of the solids' properties and their local ordering due to which establishing a short-range structure has always been the main goal of study. The peak development of this topic of solid-state physics was reached in the third quarter of the previous century. Historically, the most attention has been given to monoatomic Si and Ge, which, it would seem, is quite conducive to our study, since carbon, silicon, and germanium form a common tetrel's family of the Mendeleev's table so that a similar behavior could be expected of all the members. As was found, tetrahedrally bonded sp^3 configured atoms form the short-range order of Si and Ge amorphous solids. However, in the case of carbon, as seen in Fig. 1*b*, similar amorphous compositions of carbon are concentrated only near

sp^3 corner and are related to the ta–C phase. This internal protest of carbon atoms against the sp3 hybridization of their electrons in the solid state is confirmed by extremely severe conditions for the formation of diamonds (40 GP and 960–2000°C) [46]. In contrast to Si and Ge, the main part of the pure C-solids is sp^2-configured. A comprehensive discussion of this peculiarity related to the tetrel's family members is outside the topic of the current review and can be found in monograph [28]. Thus, monoatomic solid carbon has the unique ability to form amorphous (as well as crystalline) states of two types, characterized by fundamentally different short-range orders presented by either tetrahedral sp^3 groups of bonded atoms or an sp^2 honeycomb network of benzenoid units, graphene domains, thus strongly differentiating sp^3 and sp^2 aCs. Throughout this review, we will mainly talk about sp^2 aCs.

Recent comparative studies [47–50], taken together with a large pool of individual data, have shown that the general architecture of both natural and synthetic sp^2 aCs is common and can be characterized as a multilevel fractal structure [36,51,52], albeit differing in detail at each level. The structure of the first level is similar in all the cases and is presented by necklaced graphene BSUs introduced earlier. The necklacing plays a decisive role, ensuring the formation and stability of short-range order, on the one hand, and preventing graphitization, on the other [1,2], thus allowing the attribution of the sp^2 aCs origination to the reaction amorphization [3]. The second-level structure is provided with nanometer-thick BSU stacks, which were confidently recorded by X-ray and neutron diffraction structural studies of sp^2 aCs of all types [48]. Once standard, BSU stack pattern forces us to expand the amorphics' short-range order, completing individual BSUs with their stacks and thus distinguishing sp^2 aCs from routine molecular amorphics [4,53,54]. The third-level structure of the amorphics reliably follows from the porous structure evidently observed experimentally [52,55]. It is constructed from the BSU stacks but the final compositions depend on the stacks' lateral dimension. When the latter is at the first nanometers level, the composition presents globules of ~10 nm in size, which well correlates with pores, the size of which is first nanometers as well [52,56]. Further aggregation of globules leads to the formation of micro-nanosize agglomerates with pores of tens nm and more [52]. Such a structure is typical to natural sp^2 aCs such as shungite carbon, anthraxolite, anthracite, as well as black carbon coating of diamonds [57], mixed carbon-silica spherical 'sweets' [58], black carbon in meteorites [59,60] and metamorphosed polymictic sandstones [61], biogenic carbon, originated from anaerobic oxidation of methane [62], and none of the exclusions have been known so far. **Fig. 2** presents the evolution of the structure of this kind of sp^2 aC from a single BSU to macroscopic rocks. A schematic structure of a globule, shown in the figure, is designed on the data related to shungite carbon. Molecule $C_{66}O_4H_6$ constitutes one of the possible models of the BSUs based on the graphene domain

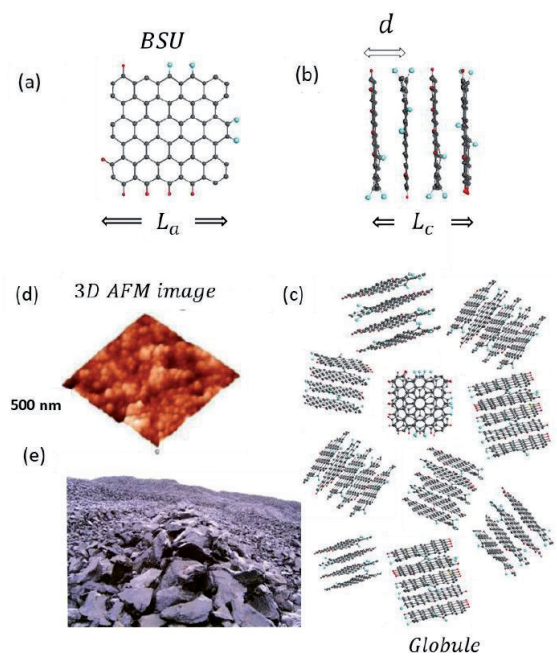

Fig. 2. *Multi-level structure of sp^2 amorphous carbons, BSU size of which constitutes first nanometers. (a) Single necklaced-graphene BSU ($C_{66}O_4H_6$ for shungite carbon* [36]*). (b) Four-layer BSU stack. L_a and L_c are linear size of BSU and BSU stack thickness of 1.2 nm and 1.4 nm, respectively; d is interlayer distance of 0.35 nm. (c) Planar view on a model globule composed of different stacks, the latter consisting of BSU layers from 4 to 7, differently oriented to each other, with total linear dimensions of ~ 6 nm [1]. Gray, red and blue balls depict carbon, hydrogen, and oxygen atoms, respectively. (d) 3D AFM image of globular structure of shungite carbon powder* [36]*. (e). Karelian shungite carbon deposit* [63]

C_{66} [49]. The model is commensurate by size with real BSU and its heteroatom necklace is composed basing on chemical data of the species established in [48]. Combined into four-, five-, and six-layer stacks in accordance with empirical structural data [47–50], the molecules create a visible picture of the nanoscale globules, further agglomeration of which provides the final nanostructured view of the species presented by the 3*D* AFM image in the figure. In contrast to natural bodies, synthetic amorphics are characterized by a large dispersion of BSU size from units to tens and/over first hundreds of nanometers. At the low-limit end of the dispersion, their structure is similar to that of natural species described above. At the high-limit end, the BSU size does not prevent from BSU packing in nanosize-thick stacks while the latter laterally extended are further packed in a paper-like structure. The above concept concerning sp^2 aCs structure is based on planar BSUs. The latter are indeed characteristic of real structures, evidence of which are numerous. However, from time-to-time images of natural solids exhibit bent fragments. The issue will be discussed in Section 3.2.

As mentioned earlier, sp^2 aCs do not match any of the known types of disorder that are characteristic for monoatomic covalent solids [3]. Considering this, the sp^2 carbon amorphization can be attributed to enforced fragmentation of graphite [36]. Obviously, fragmented product can be obtained from both the top and bottom. In the first case, it means the disintegration of pristine graphite, while in the second case, it concerns stopping the graphitization of pristine graphene lamellas. There might be various reasons for fragmentation, including mechanical impact, chemical reaction, temperature shock, exposure to hard radiation, etc. However, each fragmentation act is completed with a chemical reaction providing stabilization of necklaces around fragmented graphene domains. Thus formed BSUs, mainly, and their stacks, additionally, ensure the short-range order of the sp^2 aCs. They are characterized by large variety with respect to not only different classes of aCs, but to the same class as well. The variety concerns the BSU size, shape, variation of necklace chemical content, and, most importantly, the local distribution of heteroatoms in the BSU necklaces at fixed atomic percentage on average. Thus, to complete empirical analytics of sp^2 aCs with a virtual one, a large family of NGMs should be associated with each real sample [64]. A single member of the family, shown on the top of Figure 2, is only 'one snapshot' of communities related to one of the possible permutations of hydrogen and oxygen atoms in the framing area.

Completing the introduction, a few words should be added about the radical nature of the sp^2 aCs BSUs. The latter is provided with chemical activity of valence uncompensated sp^2 carbon atoms, among which non-terminated edge atoms of graphene domains (these atoms of the NGM $C_{66}O_4H_6$ are clearly seen on the top of Figure 2) are the most active. In spite of this, the BSUs remain stable radicals due to the spin-delocalized character of the molecule radicalization provided by the conjugation of unpaired sp2 electrons over the total number of carbon atoms, nearly degenerated spin-triplet energy gap E_{ST}, incorporation of heteroatoms (O, N, S) inside benzenoid units or outside the latter [65]. The sleeping activity of the bodies can be stimulated by the additional fragmentation [66], as is in the case of the sp^2 aCs catalytic application [67].

3. STRUCTURE OF SP² AMORPHOUS CARBONS

3.1. Short Foreword

Once started as classical continuous bulks, today's sp^2 aCs unhesitatingly take their place among nanotechnological materials. Their scientific perception was developing alongside the growing material science, receiving at each turn of the progression a stimulating pulse of a deeper penetration into the understanding of their nature. This development, support, and stimulation would not have been possible without simultaneous progress of instrumental analytical technology. Such a coordinated movement clearly manifested itself to be applied to the structural studies of sp^2 aCs. A perfect historical review on the structure of carbon materials explored by local transmission electron microscopy and global powder diffraction probes [68] presents this growth in the best way. A set of modern techniques, suitable for studies of the structure of nanomaterials, includes atomic force microscopy (AFM), scanning electron (SEM), scanning transmission electron microscopy (STEM), high-resolved transmission electron microscopy (HRTEM), X-ray powder diffraction (XRPD), and thermal neutron powder diffraction (NPD). All these

methods have their advantages and disadvantages, and none of them is sufficient to completely disclose the sp^2 aCs structure. The best success is achieved with the joint use of electron microscopy (EM) and powder diffraction (PD) [68]. It is this combination which will be the focus of this review as well.

Structural studies of sp^2 aCs are obviously complicated by the multilevel structure of a real object. Starting from the bottom, the amorphic structure gradually becomes more complex from individual BSUs to BSU stacks, then to globules of aggregated stacks, and finally to micro- and/or macro-scopic agglomerates. None of the analytical methods described above "sees" the structure of the matter in its entirety. Thus, individual BSUs, which are molecular entities, are not atomically seen by any of the methods. Only HRTEM makes it possible to detect the presence of individual BSUs of first nm in size as bar-like images of vertical projections of the areas occupied by carbon atoms. Simultaneously, HRTEM reveals the presence of BSUs' stack structure thus making possible to estimate the degree of turbostraticity in the latter [69,70]. If the corresponding microscope is equipped with a console that provides fixation of the electron beam diffraction on the sample, then it may determine the interlayer distance d inside the stacks of BSUs [13]. In the number of cases related to medium-resolution either TEMs or STEMs, it is possible to reveal well-structured globules of 10–20 nm in size. Images obtained with submicron-resolution EM instruments, as well as with AFM, represent the samples under study in the form of microscopic agglomerates. It should be taken into account that all EM methods deal with a strictly limited part of the object under consideration. All the obtained results are local and may change, sometimes significantly, when passing to another place of the studied sample.

XRPD and NPD are powerful techniques related to samples as a whole. However, they concern the stack structure only, but allow determining not only interlayer distance d inside the stacks, but linear dimension L_a of BSUs, that constitute the stacks, as well as thickness of the latter L_c (see the description of the values in Fig. 2). Because of significant variability of the sample amorphous structure, the obtained data are statistically averaged and may differ from local ones, obtained microscopically.

Summarizing this short foreword in terms of amorphous state physics, we may state that the modern structural techniques can distinguish short- and middle-range order of solid sp^2 aCs, but in different way. Thus, HRTEM sees the former quite definitely, both as individual BSUs and as stacks of them, but quite locally with respect to the sample body. STEMs of high resolution may visualize the second one as globules of stacks, also locally. Both PD techniques visualize the short-range order in statistically averaged values of the interlayer distanced d in stacks, the stack thickness L_c, and linear dimension of BSUs L_a, composing the stacks [69]. In what follows, a representative set of sp^2 aCs will be presented in light of EM an PD techniques applied together. This investigation concerns a set of samples listed in Table 1.

3.2. Electron Microscopy

Fig. 3 presents a collection of EM results that demonstrate the analytics ability. A comparative view of the images presented in Fig. 3*a–c* allows seeing that microscopic particles of the solids have a common inner structure based on nanosize elements. At the same time, the structures themselves are quite different, apparently evidencing different characteristics of aggregation that precede the solidification. Evidently, the latter occurs differently in nature (cf. Fig. 3*a,b*) while being similar in nature

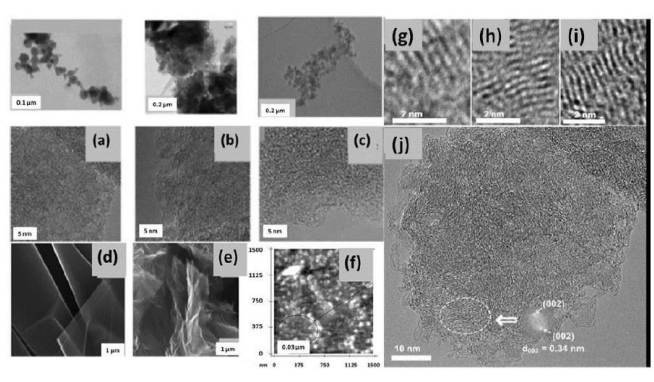

Fig. 3. *Multilevel structure of sp^2 amorphous carbons in light of electron microscopy. (a–c) STEM (top) and HRTEM (bottom) images of ShC (a), AnthX (b), and CB of Sigma-Aldrich-Merk (c). (d) and (e) SEM images of paper-like technical graphenes Ak-rGO (d) and TE-rGO (e). Adapted from Ref. [49]. (f) SEM image of globules' aggregates [7]. (g–j) HRTEM images of the atomic structure of ShC: stacks of flat (g-h) and bent (i) BSU layers. General view of a ShC particle (j), for which Fourier diffraction pattern of the indicated area (see inset) was obtained. Adapted from Ref.* [13]

and industry (cf. Fig. 3*a,c*), and again differently when going from industrial production of carbon black to chemically synthesized Ak-rGO and TE-rGO (cf. Fig. 3*c–e*). In the latter case, both GO and rGO often present paper-like solids [42]. At the same time, HRTEM studies of these solids reveal a picture similar to those shown in Fig. 3*a–c*.

When EM, used earlier to study shungite carbon [71,72] in particular, did not allow for establishing the multilevel structure of sp^2 aC unambiguously, today the possibility of using it with different magnifications makes it possible to reliably verify this. This can be traced when looking at Fig. 3*a,f*. As the resolution increases, the structure of microparticles (conditional fourth level of the ShC structure) in Fig. 3*a* is replaced by aggregation of globules with an average size of tens nm (third-level structure) in Fig. 3*f* and then by a set of elements of the first nanometers in size (second- and first-level structure) in Fig. 3*a*. Similar globular images were observed for anthraxolites as well [73,74].

Fig. 3*g–j* present a detailed view of the first two-level structure of shungite carbon [13]. Bars from several fractions of a nanometer to several nanometers long are clearly visible in these images. They are the projections of carbon atom planes oriented almost parallel to the electron beam. It is clearly visible that these structural fragments are grouped into stacks. The distance between fragment planes in the stacks was estimated using a tight connection between the HRTEM image and diffraction of the electron beam providing Fourier diffraction patterns of the former [75]. Thus, the selected region in the HRTEM image in Fig. 3*j* has a Fourier diffraction spot pattern, which corresponds to the interlayer spacing (d = 0.34 nm) of a disordered graphite-like material [13].

The atomic planes grouped into stacks of 4–7 layers are clearly visible in Fig. 3*g–i*. As is seen, flat fragments are indeed characteristic of the real structure and are numerous. However, the images also contain bent fragments. Since interlayer spacing d for bent fragments is usually 0.34–0.38 nm, any chemical modification of BSUs within their basal planes, which might cause the bending, should be excluded. Accordingly, it was suggested to explain the bending of primary flat BSUs by the existence of various mineral inclusions outside the units. In fact, such impurities accompany ShC formation (from silica micro- and nanoparticles to metal nanoparticles

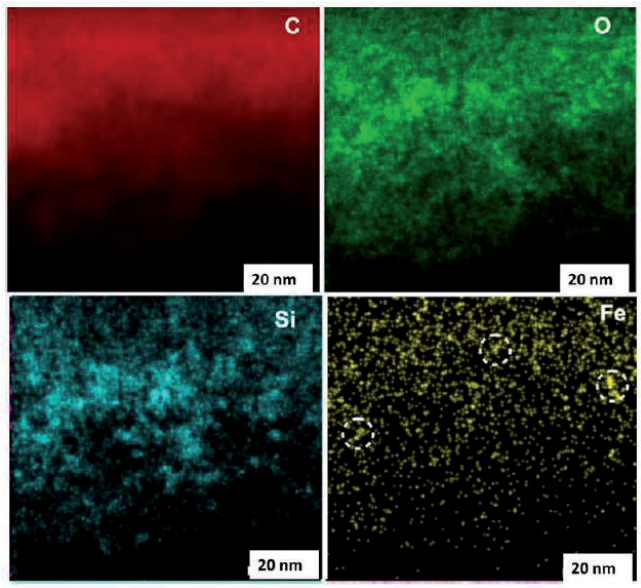

Fig. 4. *HRTEM element mapping of sp^2 amorphous carbons. Shungite carbon in the light of C, O, Si, and Fe elements. The circles in the iron map indicate nanoclusters.*

[7]). Proving the suggestion has revealed a unique opportunity of HREELS to study the atomic structure and the elemental composition of the substance under study. The latter can be disclosed when EM is combined with point-like energy dispersive spectral (EDS) analysis. **Fig. 4** presents an example of the ShC elemental composition mapping with respect to C, O, Si, and Fe constituents. It is seen that only carbon is uniformly distributed throughout the sample, whereas other elements are heterogeneously dispersed. The iron map attracts a particular attention revealing cluster segregation of fractions of a nanometer in size. Similar clusters, containing other metals, are observed as well. Primary BSUs may willingly cover metal nanoparticles and bend, similarly to graphene sheet placed on a heap of gold nanoparticles [76].

3.3. X-Ray and Neutron Powder Diffraction

X-Ray diffraction and elastic neutron scattering are widely applied to determine short-range order parameters of amorphous materials [77–79]. **Fig. 5** presents a typical set of data that provide such structural data relating to sp^2 aCs that concern BSU stacks and BSUs themselves. As is known, diffractogram reflexes Gr (*00l*) are mainly sensitive to the interlayer distance in graphite-like bodies while Gr (*hk0*) ones involve information related to graphite-like structure in the layer plane [68]. As seen in Figure 5*a,b*, all the plottings are similar and

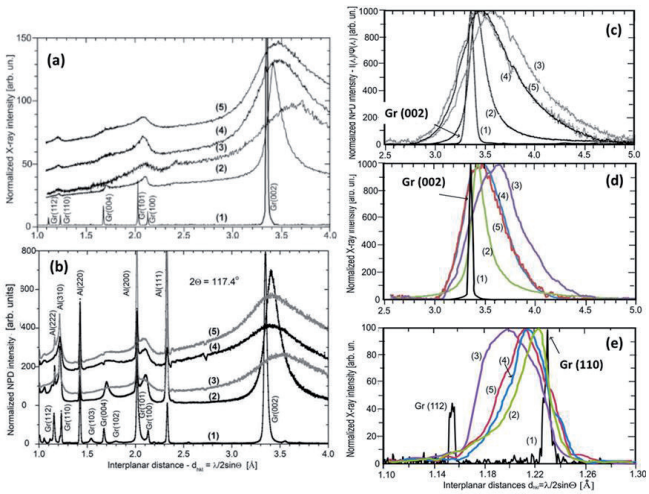

Fig. 5. *Powder diffraction in the service of short-range structure determination of sp^2 amorphous carbons. (a) Panoramic views of XRPD plottings of sp^2 aCs and graphite. (b) The same related to NPD. (c) Normalized intensities of the NPD Gr (002) reflexes. (d) The same concerning XRPD. (e) Normalized intensities of the XPRD Gr (110) reflexes. (1)–(5) mark Gr, CB624, CB632, ShC, and AntX. See the sample nomination in Table 1 and plottings details in Ref. 48. Graphite of Botogol'sk deposit* [81] *was used as standard.*

quite scarce, once expectedly concentrated around reflexes Gr (*002*). The abandon richness of NPD spectrograms is usually provided with numerous additional reflexes caused by neutron scattering in crystalline aluminum of a cryostat (see detailed comments in Ref. [80]). Gr (*002*) reflexes are located in the region of 3.3–3.5 Å, which determines interlayer distance d along c axis between the neighboring layers in graphite thus pointing to undoubted graphite-like stacking of the relevant BSUs. No less important are reflexes Gr (*110*), located in the region of 1.1–1.3 Å, which characterize the size of BSU stacks in lateral directions [69,70]. As seen in the figure, for all the studied sp^2 aCs Gr (*002*) and Gr (*110*), reflexes are shifted (up and down, respectively), as well as considerably broadened, pointing convincingly to a considerable size restriction for the relevant BSUs in both directions.

The broadening of diffraction reflexes is usually attributed to the narrowing of the coherent scattering region (CSR) of a scatterer in the relevant direction [82–84]. According to Scherrer's formula, the full width at half maximum (FWHM) of diffraction peak B and the CSR length L_{CSR} are inversely connected:

$$L_{CSR} = k\lambda/B\cos\Theta. \quad (1)$$

where λ and Θ are the neutron and/or X-ray wavelength and scattering angle while k is a factor depending on the reflex under study [82]. The factor determination is a permanent problem of a quantitative diffraction study of nanosize objects. However, when the study is performed for a set of samples under the same conditions, L_{CSR} can be addressed to the reference one as [80]:

$$L_{CSR} = (B_{ref} / B)(\lambda / \lambda_{ref})L_{CSR}^{ref}, \quad (2)$$

where, L_{CSR}^{ref}, evidently attributed to crystalline graphite, constitutes ~20 nm along both c and a directions [85].

A comparative view of Gr (*002*) and Gr (*110*) reflexes of sp^2 aCs is presented in Fig. 5*c–e*. As seen in Fig. 5*c,d*, NPD and XRPD reflexes Gr (*002*) are similar. Gr (*110*) reflexes are less intense and quite noisy due to which the usual abandon richness of NPD seriously prevents accurate working in the place while XRPD reflections remain accessible. **Table 2**

Table 2

Parameters of the short-range structure of sp^2 amorphous carbons[1].

Samples	d (Å)	L_c, nm	Number of BSU layers	L_a nm	Ref
ShC	3.47(n); 3.48(X)	2.5(n); 2.0(X)	7(n); 5–6(X)	2.1(X)	[48]
AnthX	3.47(n); 3.47(X)	2.5(n); 1.9(X)	7(n); 5–6(X)	1.6(X)	[48]
AnthC (Donetsk)	3.50(X)	2.2(X)	5–6(X)	2.1(X)	[49]
Ak-rGO	3.50(n)	2.4	7(n)	>20	[5]
TE-rGO	3.36(n)	2.9	8(n)	>20	[12]
CB632	3.57(n); 3.58(X)	2.2(n); 1.6(X)	6(n); 4–5(X)	1.4(X)	[48]
CB624	3.40(n); 3.45(X)	7.8(n); 4.1(X)	23(n); 12(X)	2.5(X)	[48]
μncr Gr	3.35	>20	~100	>20	[48]

[1]Notations (*n*) and (*X*) indicate NPD and XRPD data, respectively; [2]The definition "> 20 nm" marks the low limit of the dimension pointing that it is bigger than the CSR of crystalline graphite equal to ~20 nm along both a and c directions. Actual dimensions are of micrometer range.

accumulates L_c and L_a data, determined by applying Equation (2) to the obtained data. As seen in the Table, maximum positions, *d*, of Gr (*002*) reflexes, provided by NPD and XRPD measurements of the studied aCs convincingly evidence that all the samples consist of stacks formed by graphene-like BSUs. The average interlayer distance in the stacks constitutes $d = 3.47 \pm 0.10$ Å, thus remarkably exceeding *d* in graphite crystals. This was to be expected, since the components of the BSU stacks are not flat one-atom-thick bare graphene domains, but NGMs. The van der Waals thickness of the necklace heteroatoms and their possible deviation from the domain plane is the main reason for the increase in this standard graphite parameter.

4. GENERAL ATOMIC CONTENT OF SP2 AMORPHOUS CARBONS

4.1. Short Foreword

Since BSUs are responsible for the short-range order of sp^2 aCs, it is these bodies that govern the chemical content of the whole solid. Evidently, the presence of BSUs' necklaces determines the unavoidable heterogeneity of the latter. The necklace contribution into the total atomic content is structure-sensitive. It gradually decreases from a few at % to a negligible amount when the BSU size grows from the first nanometers to micrometers. As seen in **Table 2,** BSUs of the selected set of sp^2 aCs are nanosize to be proper for heterogeneous chemical analysis. Modern analytic techniques are usually specified for the determination of particular sets of elements. Carbon, hydrogen, and oxygen are the main triad of organic chemistry, so that their dominant presence in the aCs is fully expected. Analyzing the available assortment of analytic techniques, one can make sure that practically all of them are able to fix carbon. As for hydrogen and oxygen, the techniques are distinctly divided into {C,H}, {C,O}, and {C,H,O} groups. Following this division, we subordinate further description to this grouping.

4.2. {CH} Analytics

Analytic techniques are qualitative, quantitative, or mixed. The first are those based on chemical or physical properties that reveal a strong dependence on the chemical entity under study. In the case of sp^2 aCs, combustion and incoherent inelastic neutron scattering (IINS) of hydrocarbons are widely used for detecting hydrogen. The former lays the foundation of differential thermal analysis (DTA) and differential scanning calorimetry (DSC) [86], the latter, less popular, presents inelastic incoherent neutron scattering (IINS) vibrational spectra [87].

The DTA/DSC analysis mainly concerns the *brutto* content of sample carbon, so called *fixed carbon* following the equation

$$\% \text{ Fixed Carbon} = 100 - (\%\text{Adsorbed Water} + \%\text{Ash} + \%\text{Volatile Matter}) \quad (3)$$

The fixed carbon is definitely not carbon-pure and must at least include hydrogen and oxygen components, which are highly combustible constituents in addition to carbon. As occurred, DSC thermograms of a set of sp^2 aCs, obtained at the same conditions, are quite different [48] while the carbonization of all the samples is over 90%. **Fig. 6***a* presents the data collection, which evidently

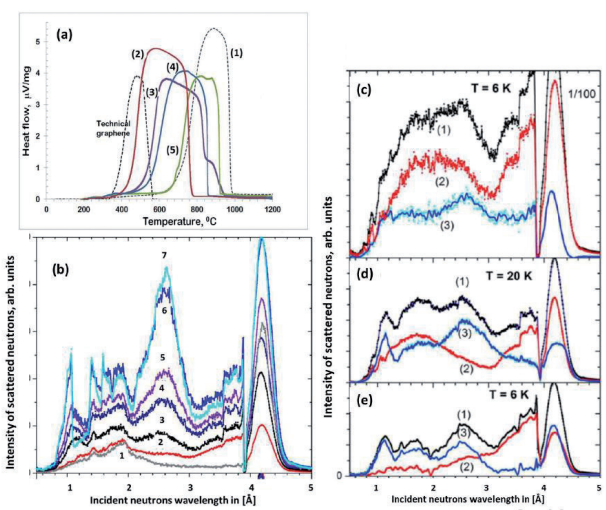

Fig 6. *Hydrogen detection in sp^2 amorphous carbons. (a) DSC thermograms of as prepared solids: spectral Gr (1), ShC (2), AntX (3), CB632 (4), and CB624 (5) [48]. DSC curve of the lab rGO is reconstructed from experimental data presented in Ref. [88]. (b) Time-of-flight IINS spectra of water gradually added to CB632. 1, 2, 3 mark scattering from Al-cryostat, dry and as prepared samples, respectively. (4–6) Spectra of water loaded in 100g of as prepared CB632 sample in ml: 0.5 (4), 1.0 (5) and 2.0 (6). (7) 2.5 ml of water loaded in as prepared CB624 sample. (c)–(e) Normalized TOF IINS spectra of sp^2 amorphous carbons after subtracting the Al-cryostat background: AntX (c), ShC (d), CB632 (e). Digits mark spectra of as prepared (1) and dry (2) samples as well as adsorbed water (3), the latter obtained as the difference between spectra (1) and (2) (see details in* [47]).

reveals changes in the temperature of the process onset T_{ost}, from 370°C to 720°C. Thus, as seen in the figure, T_{ost} of graphite is the largest. In contrast, on the opposite side of the observed series of the DSC thermograms, there is one related to a lab-produced rGO [88], Tost for which constitutes 370°C. As is known, rGOs, both natural and synthetic, usually contain a few wt% of hydrogen. Accordingly, the presented DSC series may evidence a gradual depletion of hydrogen content in the sp^2 aCs series from ShC to CB624 and graphite. In this case, the T_{ost} below 720°C obviously indicates the hydrogen presence in the solid, therewith, the lower the T_{ost}. DTA/DSC are fully qualitative techniques. However, a comparative study of a set of samples under equal conditions allows for disclosing a solids' comparable series following the decrease in hydrogen content, such as the following:

rGO > ShC > AntX > CB632 > CB624 > Gr.

In its turn, protium is a peculiar hydrogen isotope of the largest cross-section for the IINS among all the elements, making the relevant techniques highly protium sensitive. The abundance of a real hydrogen isotope family with protium readdresses the statement to chemical hydrogen [87]. Thus, water is willingly adsorbed with both natural and synthetic sp^2 aCs, which is evidently caused by their porous structure and hydrophilic nature of the BSUs necklaces that cover inner walls of pores. Expectedly, Fig. 6*b* presents a strong reaction of IINS spectra on the gradual hydration of CB632. As shown in Fig. 6*c–e*, each as-prepared sp^2 aCs involves a large quantity of adsorbed water and must be freed from it before analysis for the hydrogen content. In their turn, dry samples of the latter still remarkably scatter neutrons, thus exhibiting the hydrogen presence in the solids related to the necklaces of their BSUs. So far, none of IINS' quantitative analyzes for hydrogen in sp^2 aCs has been developed, leaving it mainly qualitative. However, when a study of a solids' set under equal conditions is possible, a comparative analysis of the obtained IINS spectra, as is in the case presented for dry samples in Figure 6*c–e*, allows a confident conclusion that the hydrogen content in the AntX and ShC BSUs is comparable, while that one for the CB632 is much lower. The relevant comparative series of samples looks like the following:

ShC ≈ AntX > CB632 > Gr.

This tendency is quite similar to the one followed from the DSC data in Figure 6*a*, while not identical. Apparently, it may be caused by the fact that DSC results were obtained for as-prepared samples that could not be fully freed from the adsorbed water.

In contrast to the above techniques, a combustion-based elemental analysis (EA) can provide a qualitative hydrogen analysis of sp^2 aCs. Standard CHNS EA involves determination of carbon and hydrogen contents supplemented with the detection of nitrogen and sulfur. It does not determine oxygen content directly and the relevant data are just residual content of 100 wt% samples mass after excluding all other contributions. The hydrogen data related to the solids listed in Table 1 are presented in **Table 3.** The comparative sample series looks as follows:

AntC > AntX > TE-rGO ≈
≈ Ak-rGO > ShC > CB632 > CB624.

There is much common and different in the triad of comparative series evidencing that obtaining exact values of hydrogen content even in the same samples of sp^2 aCs is hardly possible. None of the

Table 3

Chemical content of BSUs of sp^2 amorphous carbons

Samples	Elemental analysis, wt%						XPS analysis, wt%			
	C	H	N	O	S	Ref.	C	O	Minor Impurities	Ref.
ShC	94.44	0.63	0.88	4.28	1.11	[48]	88.5	8.6	2.9	[48]
AnthX	94.01	1.11	0.86	2.66	1.36	[49]	89.5	7.7	2.8	[48]
AnthC	90.53	1.43	0.74	6.44	0.89	[49]	89.6	8.1	2.3	[49]
TE-rGO	84.51	1.0	0.01	13.5	1.0	[49]	82.3	14.8	2.9	[49]
Ак-rGO	89.67	0.96	0.01	8.98	0.39	[49]	89.5	7.6	2.9	[49]
CB624	89.67	0.18	0	0.15	-	[48]	93.1	5.9	1.0	[48]
CB632	97.94	0.32	0.04	1.66	0.68	[48]	90.7	7.8	1.5	[48]

techniques are free from particular limitations related to both the performance and interpretation of the results obtained. However, all of them are highly important and useful.

4.3. {CO} ANALYTICS

Since CHNS EA does not provide the determination of the oxygen content, EDS and X-Rays photoelectron spectroscopy (XPS) take on the main role. Both techniques are qualitative and quantitative, thus detecting the oxygen presence in samples and determining its atomic percentage. **Fig. 7** presents a general view on these techniques' abilities. Qualitative EDS, known as EDS mapping, allows for registering of the distribution of a selected element over the sample by monitoring its monochromatic X-ray emission [89]. Typical EDS maps for ShC are presented in Fig. 7*c–e*. As seen in Fig. 7*e*, oxygen is largely presented in the solid. The quantitative EDS analysis (Fig. 7*a*) concerns a comparison of the intensity of element-wave-dependent X-ray emission with that of a standard reference element registered at identical conditions. A characteristic feature of EDS is the localized

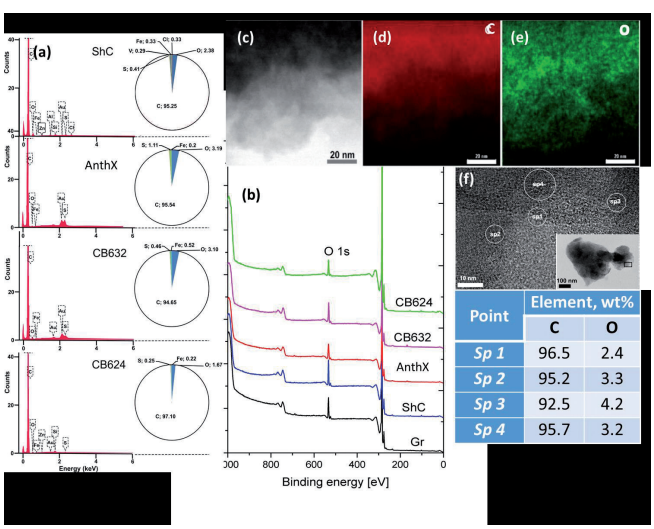

Point	Element, wt%	
	C	O
Sp 1	96.5	2.4
Sp 2	95.2	3.3
Sp 3	92.5	4.2
Sp 4	95.7	3.2

Fig. 7. *Oxygen detection in sp^2 amorphous carbons. (a) EDS spectra and content diagrams of dry sp^2 amorphous carbons. Spherical diagrams visualize the samples chemical content, details of which are given in Ref.* [48]. *(b) XPS survey spectra of as prepared amorphous carbons and graphite GSM2 at room temperature* [48]. *(c)–(d) Dark-field HRTEM of an edge fragment of ShC particle (c) and its element EDS mapping for C (d) and O (e) elements. (f) Localization of EDS point elemental analysis of ShC, the data of which are listed in table below. The inset marks the region under study. Details are given in* [13].

character of its data. The measurements are usually performed at inclusion-free sites controlled by EDS maps, similar to the O-map in Fig. 7*e*. The data should be averaged over those determined at several different places for each sample. As shown in Fig. 7*f*, the data related to different places of the sample scatter quite remarkably. Fig. 7*a* presents a collection of EDS spectra of a set of dry sp^2 aCs samples while partitioned chemical components are presented by spherical diagrams. As seen in the figure, the emission spectra are presented by main signals related to carbon, the amount of which covers the region of 95.05÷97.44 wt%, and oxygen of 1.7÷3.3 wt%. In addition, a variable set of minor impurities is usually obtained. EDS analysis confirms that sp^2 aCs are not carbon-pure but involve a few percentages of oxygen and ~1.5 wt% of minor impurities.

In contrast to EDS, XPS data are statistically space-averaged. A general panorama of the survey XPS spectra of a set of sp^2 aCs is presented in Fig. 7*b*. It is usually assumed that a high degree of vacuum provides the release of the studied samples from the adsorbed water. Quantification of atomic content is provided using sensitivity factors from the elemental library of CasaXPS [90]. The XPS spectra of the studied samples look quite similar, evidencing the C1s and O1s spectra of the main chemical components and allowing for the evaluation of atomic percentage of the observed elements by standard technique. The obtained data are given in Table 3. As seen in the table, all the studied sp^2 aCs contain a considerable amount of oxygen.

Concluding the chemical testing, is necessary to pay attention to the following: all the methods allow for the direct determination of carbon content. The dispersion of the latter occurs quite largely and constitutes 95.2÷88.5 wt% for ShC, 95.6÷89.5 wt% for AntX, and 97.94÷90.7 wt% and 99.67÷93.1 wt% for CB632 and CB624, etc., respectively. This feature clearly evidences the multi-elemental character of the species, on the one hand, and the different sensitivity of the used analytical techniques to chemical elements that accompany carbon in the studied samples, on the other. It is important to note as well that all the reference carbons unavoidably used in testing are not pure carbons as well. Oxygen is the main impurity, which may point to a heightened propensity of pure carbons to

oxygenation. Hydrogen is the next contributor. In addition, the hydrogen weight content is comparable with that of other minor impurities involving sulfur, nitrogen, chlorine, silicon, and different metals. The role of the latter is particularly important in the geochemistry of carbon [91,92] or the engineering technology of highly carbonized products [93]. Once concentrated on disclosing the BSU atomic structure, we shall restrict ourselves in what follows by the consideration of carbon–hydrogen–oxygen triad that present necklaced graphene oxyhydrides. The latter are covalent species characterized by a large variety of covalent bonds between the triad elements, attribution of which to particular atomic pairs is provided with the {CHO} analytics of sp^2 aCs.

4.4. {CHO} Analytics

There are many methods for the direct or indirect determination of the composition of covalent bonds. As applied to sp^2 aCs, the most successful are vibrational spectroscopy in the first case and XPS in the second. Vibrational spectroscopy includes a wide range of different methods based on the inelastic scattering of elementary particles (photons, neutrons, electrons, γ particles, neutrinos, etc.). Each of these methods is characterized by its own way of extracting information about the covalent bonds of a scattering substance from the corresponding spectra. Methods for the indirect study of the bonds are based on the reaction of the binding energy of atoms to the presence of other atoms bound to them, the most prominent representative of which is XPS. This method is widely used in the analytics of sp^2 aCs, and that is why we will begin the review of {CHO} analytics with it.

4.4.1. XPS analysis

In contrast to IINS, which is a 'hydrogen tool' and which provides a reliable qualitative test of the hydrogen presence in sp^2 aCs, XPS in general, and its O1s spectra in particular, is considered as the main 'oxygen tool' of the solids. The determination of O/C content, exhibited in Figure 7*b*, is usually followed with a detailed analysis of covalent bonds, formed by the element within the bodies' BSU necklaces. **Fig. 8** presents a general view on a massive set of XPS results, for a selected set of sp^2 aCs listed in Table 1. As mentioned earlier, XPS analysis of chemical bonding is based on

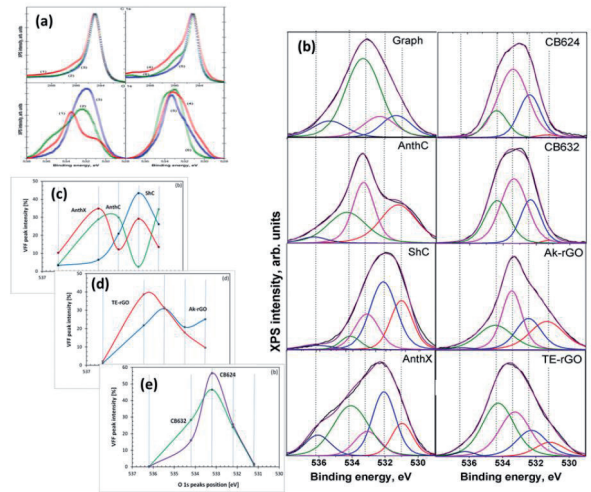

Fig. 8. *sp^2 Amorphous carbon chemical bonds configuration in view of XPS. (a) C1s (top) and O1s (bottom) XPS spectra of AnthC (1); AnthX (2); ShC (3); TE-rGO (4), Ak-rGO (5) and CB632 (6) at room temperature. (b) Expanded O1s XPS spectra and fraction-distributions of Voigt-fitting-function (VFF) peaks of O1s spectra over peaks number of natural (left) and synthetic (right) sp^2 amorphous carbons at room temperature. (c)–(e) Distribution of the VFF peaks intensity over group binding energies for natural (c), synthetic (d) and industrial (e) sp^2 aCs. Details are presented in* [49].

two fundamental facts: (1) the atom-dependent value of binding energy (BE_A) of electrons on internal orbits of the *i–th* atom, BE_{iA}; and (2) the BE_{iA} value's dependence on the *i–th* atom neighboring, which allows disclosing the type of chemical bonding of the atom to other ones. Both features are clearly visible in the case of sp^2 aCs carbon (C1s) and oxygen (O1s) XPS spectra shown in Fig. 8*a*. The tailing of C1s spectra and broad O1s ones are commonly associated with the multi-variable response of carbon and oxygen atoms to their surroundings. For a long time, the relevant XPS spectra have been analyzed in terms of the 'four peaks' approximation that involves groups C–C, C–O, C=O, and COO of C1s spectra and C–O, C=O, C(=O)O, and O=C(O) groups of O1s spectra [94–104]. In the latter case, the corresponding components are usually associated with the simplest oxygen containing groups (OCGs) such as hydroxyls, epoxides, carbonyls, and carboxyls. The approach resulted from the extended XPS study of numerous different polymers of known structures, which laid the foundation for atomic group assignment

Table 4

Group binding energies of O1s XPS spectra attributed to BSUs of sp^2 amorphous carbons (composed from the published data [113]).

GBEs	BE, eV	Assignments
1	531.2	C=O, O=C-O-C=O, O=C-O-C (lactones and pairs of lactones)
2	532.2	O=C-O-C (lactones); O=C-C=O (o-quinones); O=C-OH; C=O in aggregated cyclic ethers with lactone
3	533.2	sp^2C-OH; C-O-C in cyclic ethers; C-O-C-OH (hydroxypyrans: singles and pairs); O=C-O-C (lactones and pairs of lactones); O=C-OH; C-O-C in aggregated cyclic ethers with lactones
4	534.2	C-O-C in aggregated cyclic ethers; C-O-C-OH (hydroxypyran: singles and pairs); C-O-C in aggregated cyclic ethers with lactones
5	536.2	O=C-O-C-O-C-O-C-O-C=O in aggregated cyclic ethers with lactones

to characteristic XPS peaks [105]. However, this approach happened to conflict with IR absorption studies, which revealed much more complicated OCGs, including benzenoid heterocycles such as ketones and quinones, cyclic ethers, lactones and acid anhydrides, furan and pyrans, as well as hydroxypyrans and so on [106–111]. Evident questions were raised in the case of XPS [112], the answers to which were collected in a profound review [113]. Thus, a 'five peaks' approach was suggested to decompose O1s spectra, which was realized with respect to spectra shown in Fig. 8*a* [48,49]. The modified asymmetric Voigt functions [114] were adopted to separate waveforms of XPS spectra following the group binding energies listed in **Table 4**. A full collection of the decomposed data is presented in Fig. 8*b*, while a comparative view of them relating to natural, synthetic, and industrial sp^2 aCs is shown in Fig. 8*c–e*, respectively. Thus, the revealed OCGs related to the BSUs of a selected set of sp^2 aCs are summarized in **Table 5**.

4.4.2. IINS Analysis

A high efficiency of IINS spectroscopy as an H-tool is clearly seen in Fig. 6. Original IINS spectra depend on the instrumentational peculiarities of the spectral devices in use. Accordingly, the spectra recorded either on the NERA spectrometer of the high flux pulsed IBR-2 reactor of the Frank Laboratory of Neutron Physics of JINR, or on the TFXA spectrometer at the ISIS pulsed-neutron source, Rutherford Appleton Laboratory, and on IN6 spectrometer of the ILL should be and, actually are, different. However, evidently, common information related to the vibrations of a scatterer involved in the action can be provided by converting the original data to the generalized density of vibrational states (GVDOS) by the relevant standard programs [87]. A collection of such GVDOS spectra, related to a set of sp^2 aCs listed in Table 1 [49], is shown in **Fig 9**. The spectra concern dry samples after removing adsorbed water. They are provided

Table 5

XPS-revealed oxygen-containing groups related to BSUs of sp^2 aCs, based on data of Refs, 48 and 49.

Samples	Assignments
ShC	carbonyls sp^2 C=O; acid anhydride O=C-O-C=O; o-quinone O=sp^2C-sp^2C=O, carboxyls sp^2C=OOH.
AntX	hydroxyls sp^2-OH; C-O-C-OH (hydroxypyran-HP) and pairs of HPs; C=OOC(lactone) and pairs of lactones; aggregated cyclic ethers with lactones.
AntC	carboxyls sp^2C-COOH; cyclic ethers; aggregated cyclic ethers; pyran and hydroxypyran.
Ak-rGO	aggregated cyclic ethers and aggregated cyclic ethers with lactones; lactones and pairs of lactones.
TR-rGO	aggregated cyclic ethers and aggregated cyclic ethers with lactones; hydroxypyrans and lactones, both singles and pairs.
CB632	C-O-C in cyclic ether and aggregated cyclic ether; C-O-C of pairs of cyclic ether and aggregated cyclic ether with lactone.
CB624	C-O-C in cyclic ether, aggregated cyclic ether and aggregated cyclic ether with lactone

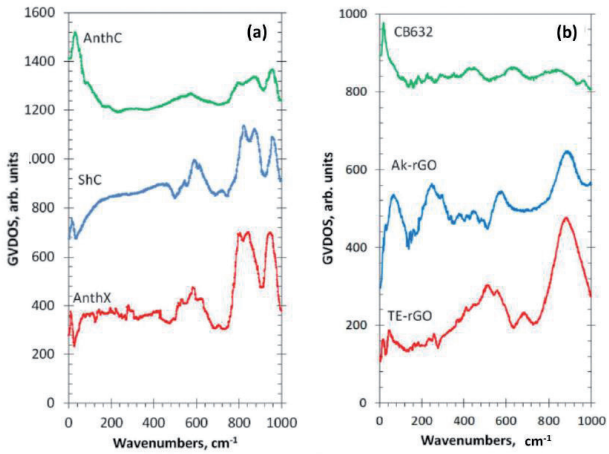

Fig. 9. *Generalized density of state of the hydrogen-involved vibrations of sp^2 amorphous carbons. (a) GVDOS spectra of dry natural solids, derived from IINS spectra at T = 20 K. (b) The same but for industrial and synthetic solids. See details in Ref.* [49].

with both direct scattering from hydrogen atoms, chemically bound with the edge atoms of the BSUs' graphene domains, as well as with enhanced scattering from the carbon atoms of the relevant graphene domains due to the 'riding effect'. The latter is caused by the contribution of hydrogen atoms to the eigenvectors of vibrations related to carbon atoms through the BSU molecules (see detailed discussion of both effects in [5]). The spectra are fine-structured enough to be attributed to particular vibrations, thus establishing the chemical bonding of hydrogen atoms in the solids [87]. As is typical for any vibrational spectroscopy of molecules, group frequencies (GFs) lay the foundation of the covalent bonds analysis [115]. Presented in **Table 6**, GFs correspond to atomic bonding inside (C,X) groups (X = C, H) [49].

The GVDOS spectra in Fig. 9 are definitely divided into two parts. Thus, all the spectra in Fig. 9*a* have much in common in the regions of 960 cm^{-1}, 800 cm^{-1}, and 600 cm^{-1} in spite of being recorded on different spectrometers, namely, ShC and AnthX on NERA [121][1] and AnthC on TFXA [122]. Characteristic spectral features are clearly visible in all the spectra, thus indicating a similar involvement of hydrogen atoms in the scattering. Table 6 accumulates group frequencies widely used in the analysis of vibrational spectra of hydrocarbons [116]. According to the table, first two features are attributed to the in- and out-of-plane bending vibrations of sp^2C-H bonds of methyne groups, while the third one represents ip bendings of carbon atoms of the benzenoid units of the BSU graphene domains enhanced by the 'riding effect'. Therefore, the IINS study of natural sp^2 aCs reveals that, in addition to the similarity in molecular spatial structure of their BSUs, hydrogen atoms in their necklaces predominantly form sets of methyne

Table 6

Group frequencies of aromatic molecules required for the hydrogen-content analysis of vibrational spectra of sp^2 amorphous carbons.

Spectral Region, cm^{-1}	Group Frequencies[1]			
	(C, C)[2]	(C, H_1)[2]	(C, CH_2)[3]	(C, CH_3)[4]
400–700	404 δ *op* C-C-C	673 δ *op* in phase	711 δ CH_2	210 *r* CH_3
	606 δ *ip* C-C-C	846 δ *op*, C_6 libration		344 δ CH_3
	707 C-C-C puckering	967 δ *op*		900 ν C-CH_3
700–1200	993 ring breathing	990 δ op, trigonal	948 ϱ CH2	1041 ϱ CH_3
	1010 δ C-C-C	1037 δ ip		
	trigonal	1146 δ ip, trigonal		
		1178 δ ip		
1200–1600	1309 ν C-C Kekule	1350 δ ip in phase	1409 δ internal CH_2	1333 δ CH3
	1482 ν C-C	3056 ν C-H		1486 δ internal CH_3
	1599 ν C-C	3057 ν trigonal C-H		
2800–3200	-	3064 ν C-H	3114 ν CH_2	2950 ν CH_3
		3073 ν in phase C-H		

[1]Greek symbols ν, δ, ϱ, r, τ mark stretching, bending, rocking, rotational, and torsion modes, respectively; [2]GFs notifications of fundamental vibrations of benzene molecule [116]; [3]GFs notifications of fundamental vibrations of benzyl radical [117,118]. Hereinafter, GFs, additional to the benzene pool of vibrations, will be shown only; [4]GFs notifications of fundamental vibrations of toluene [119,120].

sp^2C–H bonds. An intense peak below 100 cm^{-1} in the AnthC spectrum indicates that besides sp^2C–H bendings, torsions of hydroxyls take part in the scattering. A further support of the latter suggestion is given in Section 5.3.2.

In contrast to natural amorphics, their synthetic and industrial analogues are characterized by significantly different GVDOS spectra, as seen in Fig. 9*b*. A comprehensive analysis of the spectra [49] showed that the formation of methylene sp^2C–CH_2 bonds in the BSU necklaces of the solid was the main motive of the H/C bonding in TE-rGO, while the formation of sp^2C–CH_3 methyls dominates in the Ak-rGO solid. In both cases, the chemical bonding of the BSU necklaces was a direct consequence of chemical reactions that accompanied the reduction of parental graphene oxide [49]. As for the spectrum of industrial CB632, it is very weak while that of CB624 cannot be distinguished over the background at all. This feature points to a practical absence of hydrogen in their BSU necklaces and is evidently connected with the high-temperature pyrolytic conditions of the solids production, which does not maintain the existence of hydrogen-containing radicals in the chemical surrounding. The hydrogen content in CB632 is at the limit of the technique sensitivity due to which only a sharp feature below 100 cm^{-1} marks the presence of hydrogen atoms in the species BSU necklace. Apparently, it may be attributed to the presence of hydroxypyran in the area.

4.4.3. IR Absorption Analysis

Organic chemistry is unthinkable without the widespread use of IR spectroscopy as the main analytical technique. The molecular nature of BSUs of sp^2 aCs undoubtedly puts the latter on par with other objects in the field. The special significance of this type of analysis of sp^2 aCs became apparent after it was found that the heteroatoms of the BSU necklaces, chemically bonded to the graphene domain, make the main contribution to the solids IR absorption spectra [64]. This feature will be discussed in more detail in Section 5.3.2. FTIR and DRIFT techniques are usually used to record the IR absorption spectra of the solids.

DRIFT spectra of sp^2 aCs listed in Table 1 are presented in the top panels of **Fig. 10**. They are combined in groups related to natural, synthetic, and industrial solids. A large variety of the spectra shape convincingly evidence a drastic variation of the chemical content of BSU necklaces of the solids. Evidently, to proceed with the spectra features assignment, a list of GFs related to the (C, O) bonding is needed. Such a list, based on the assignment of frequencies in the experimental spectra of graphene oxides [106,109,113,123] and extended calculations [64,124], is given in **Table 7**. As seen in the Table, practically each spectral region of the spectra is quite ambiguous, which complicates the assignment. However, a combined analysis of IR and XPS spectra greatly facilitates the job. The bottom panels in Fig. 10 present the distribution of the intensity of the Voigt fitting function (VFF) peaks (see Fig. 8*b*) over group binding energies related to oxygen O1s state. The relevant GBEs are listed in Table 4.

A joint DRIFT-XPS analysis of the studied sp^2 aCs shows that the features of these spectra can be described by taking into account the hydrogen and oxygen components of the BSUs' necklaces only [49]. As for the former, it dominates in natural aCs (Fig. 10*a*), and is still significant, but is much less intense in synthetic ones (Fig. 10*b*) and is practically absent in industrial carbon blacks, approaching nil for CB624 (Fig. 10*c*). This tendency is clearly evidenced with a considerable decrease in vertical scales in the figures. In full agreement with the results of the IINS analysis, the main contribution is provided with ip and op bendings of methyne, methylene, and methyl units. It should be noted as well that the

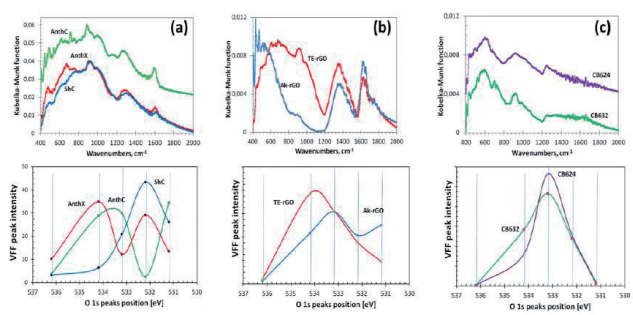

Fig. 10. *Joint DRIFT-XPS spectral analysis of sp^2 amorphous carbons. Top. DRIFT spectra of amorphous carbons at room temperature: natural (a), synthetic (b), and industrial (c) solids. Bottom. Distribution of intensities of VFF peaks of the O1s spectra of the solids presented in Figure 8b over group binding energies listed in Table 4. Adapted from* [49].

Table 7

Group frequencies required for the oxygen-content analysis of BSUs of sp^2 amorphous carbons[1], cm^{-1}.

300–1000	1000–1200	1200–1300	1300–1500	1500–1600	1600–1700	1800–1900	2600–3000	3000–3600
δ *op*², δ *ip*³, τ C-OH sp^2C-O-C and sp^2C-OH δ *op* sp^2C-C-C⁴ δ *ip*, puckering, ring breathing, δ trigonal sp^2C-C-C⁴, collective vibrations of graphene domain atoms⁵	ν sp^2C-O-C in cyclic ether, aggregated cyclic ether and acid anhydride	ν·sp^2C-OH, in lactone, hydroxyl pyran and acid anhydride	δ *ip* sp^2C-OH, ν sp^2C-O-C in cyclic ether and acid anhydride δ *ip*O-C=O in acid anhydride	δ *ip* sp^2C-OH, ν sp^2C-C	ν sp^2C =O in acid anhydride and lactone, aggregated cyclic ether with lactone pair, pairs of lactones	ν sp^2C =O in *o*-quinone, COOH	ν sp^3C-O-H in COOH ν sp^3C-H	ν sp^3C-O-H

[1]Greek symbols τ, δ and ν mark the molecule torsions, bendings and stretchings, respectively; [2]Out-of-plane bendings; [3]In plane bendings; [4]Benzene molecule data [116]; [5]Virtual data for nanographene [125].

hydrogen contribution to DRIFT spectra of natural solids is three–five times more than that of synthetic ones, while the hydrogen contents of the bodies (see Table 3) are quite comparable. This feature evidences that hydrogen atoms, directly attached the graphene domain edge atoms in the former case via sp^2C-H chemical bonds, are optically much more active than those ones involved in either methylene or methyl units via sp^2C –CH_2 and sp^2C –CH_3 bonds, once distant from the BSU domains. This issue was observed in virtual IR spectra of necklaced graphene molecules as well [64,126][2].

As seen in Fig. 10, the oxygen component of the studied solids varies quite drastically, while remaining similar in the samples of each of the three types. Thus, a joint DRIFT-XPS analysis, based on the GBEs and GFs listed in Tables 4 and **Table 7**, allowed for concluding of the following [49]: the oxygen component of the BSU necklaces of ShC may mainly involve carbonyls sp^2C=O and o-quinone O=sp^2C-sp^2C=O bonds. That one of AnthX is of lactone character consisting of C=OOC (lactone) and pairs of lactones, as well as of aggregated cyclic ether with lactone. The oxygen content of AnthC is the richest, involving carboxyls sp^2C-COOH, cyclic ethers, aggregated cyclic ethers, pyran, and hydroxypyran. Aggregated cyclic ethers, aggregated cyclic ether with lactone, and lactones are common for both Ak-rGO and TE-rGO, once completed with lactone pairs in the former case and with hydroxypyrans in the second. Similarly, C–O–C in cyclic ether and aggregated cyclic ethers with lactone form the ground of CB632 and CB624, completing the former case with lactones and/or hydroxypyrans. Obtained data led to the foundation of molecular models suggested for BSUs of the studied sp^2 aCs that are discussed in Section 5.2.

4.4.4. Raman Scattering Analysis

Raman scattering analysis has become a champion among a variety of analytic techniques applied to graphene-like materials, not excluding sp^2 aCs. No articles can be published without referring to the Raman spectra of such materials. This extraordinary situation is caused by the evident exclusiveness of the spectra, a general view of which for a set of sp^2 aCs listed in Table 1 is presented in **Fig. 11**. As seen in the figure, the spectra of samples, characterized by different short-range orders and chemical contents of the relevant BSUs, are practically identical by shape consisting of three characteristic regions named *D, G,* and 2*D* [127,128]. Following the assignment suggested for Raman spectra of crystalline graphite [129], the doublet of *D* and *G* bands corresponds

to a one-phonon contribution, while 2*D* marks the region of two-phonon events.

These one-phonon and two-phonon parts of the Raman spectra in Fig. 11 are not exactly identical, as shown by detailed consideration of the spectra structure [50]. However, a characteristic doublet *D*–*G* remains highly universal. For a long time, there has not been a convincing explanation for both the deep similarity of the spectra as a whole and the exclusive character of the *D*–*G* doublet. Starting from the spectra of crystalline graphite and graphene, consisting of two narrow bands *G* and 2*D*, spectroscopists looking for the band broadening and the appearance of *D* were divided into two groups. The first group members tried to explain the features remaining in the framework of crystal spectrum concepts. This is how the idea arose about the defective origin of the *D*-band [129,130] and about the double-resonance nature of the 2D

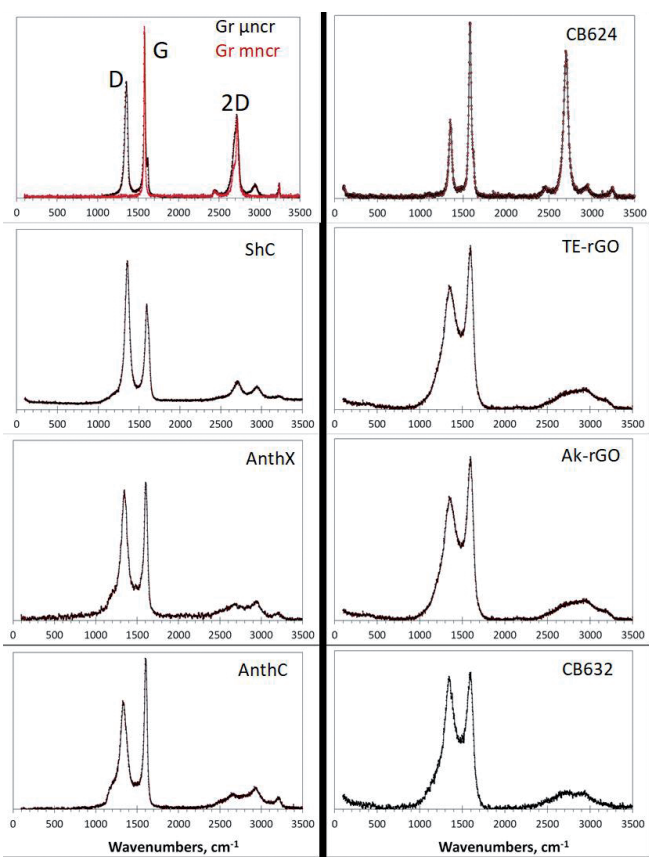

Fig. 11. *Raman spectra of sp^2 amorphous carbons at room temperature: shungite carbon (ShC), anthraxolite (AnthX), anthracite (AnthC), technical graphene TE-rGO and Ak-rGO, carbon blacks CB632 and CB624, as well as mono- (mncr) and micronanocstructured (μncr) Botogol'sk graphites, respectively (see details in* [50]).

one [131,132]. An exclusive role to two parameters of the spectra, namely the ratio of the intensity of the *D* and *G* bands, I_D/I_G , and the corresponding bands half-widths, Δω, was given to characterize the size and defect structures of the relevant graphene domains. Established theoretically for graphene crystal, this relationship was transferred to the molecular BSUs of amorphous substances by default [133,134]. However, as was shown lately [50], such a transfer turned out to be incompetent, which, nevertheless, has not stopped the efforts of the "theoretical description of the defectiveness" of the studied BUSs until now.

The molecular nature of sp^2 aCs underlies the position of scholars of the second group [135–141]. Information presented in previous sections of this article convincingly proves the issue, which makes all the crystal-based theoretical approach practically not applicable. It was shown that the polarizability tensor of a polyaromatic hydrocarbon, to which BSUs evidently belong, depends on the dynamic characteristics of the multimode vibrational spectrum. As occurred, the main contribution to the intensity of the spectra is made by sp^2C–C stretchings, due to which the observed *D*–*G*–2*D* set of bands is mainly characteristic of the network of sp^2C–C bonds. This is the first reason explaining the similarity of Raman spectra of different sp^2 aCs, since similar graphene domains constitute the main atomic part of the relevant BUSs. The second reason concerns the sp^2C–C stretching modes, which are responsible for the bands. It was found that the *G*-band is originated from the $e2_g$ vibration of benzene, while the modes responsible for the *D*-band come from the e1u mode of the molecule. The former provide simultaneous in-plane stretchings of all sp^2C-C bonds, while the latter concern both stretching and contraction of these bonds when carbon atoms move out-of-plane. A final decision of the problem has been obtained recently in the framework of virtual vibrational spectrometry [64]. As occurred, *D*-bands are, actually, caused by out-of-plane sp^2C–C stretchings that provide formation of a dynamically stimulated sp^3C–C bond between the adjacent layers of BSUs' stacks, thus being a characteristic test of a particular short-range order structure of the amorphics. Intensity of the *D*-band increases when the number of layers grows up to 4–5 and then markedly slows down when the total

thickness of stacks exceeds ~15 nm [142]. As for 2*D* region, the same out-of-plane sp^3C–C stretchings are responsible for the features, thus revealing the strongest anharmonicity among other vibrations.

A particular doublet pattern of the spectra strongly depends on the linear size of the BSU and is transformed from a broad-band-doublet one to a narrow-band one with drastic domination of the *G*-band when the size of graphene domain exceeds the free path of graphene optical phonons L_{ph} ~15 nm [143]. Therefore, the characteristic *D*–*G* doublet structure of the NGMs' Raman spectra is of structural origin, evidencing the stacked nature of the corresponding solid structure. Thus, the analysis of the structural and chemical content data, particularly, of the Raman spectra, of the cosmogenic carbon brought to Earth by the Chelyabinsk meteorite [60,144], leads to a confident conclusion about the graphite-like stacked structure of this carbon with a stack thickness of ~ 10–15 nm and more.

5. VIRTUAL ANALYTICS OF NECKLACED GRAPHENE MOLECULES

5.1. Short Foreword

Analysis of sp^2 aCs, performed using the analytic techniques described above, undoubtedly establishes the molecular nature of these solids, determines the solid-forming molecular BSUs as flattened necklaced-graphene type, estimates the average statistical linear size of them and the parameters of their primary stacking, and determines the atomic content of the BSUs' compositions. However, all these methods taken together do not allow us to describe BSUs using atomic structural forms such as $C_xH_yO_z(Imp)_{minor}$, so familiar for material science, beyond the general idea that they are graphene domains in a necklace of heteroatoms. Obviously, the numbers *x, y, z*, minor represent the realization of the chemical composition of substances, analytically determined as weight or atomic percentage, in atomic structural form. Taking into account the statistically averaged nature of the determined structural and compositional data (cf. Tables 2 and 3), the high complexity of constructing such a formula becomes evident. The first step towards solving this problem is the reduction of statistically averaged empirical data to point ones. The second step requires determining the formula-generating element and setting the absolute number of its atoms. In the case of sp^2 aCs, carbon atoms of number *x* evidently play the role. Further steps depend on which part of the BSUs is covered by this number. In the simplest case, it refers only to the graphene domain, due to which *y, z* and minor numbers determine the heteroatoms located in the BSU's necklace. If the heteroatom necklace includes carbon atoms such as those involved in carboxyl, methylene and methyl groups, or domain atoms are partially replaced by heteroatoms as in the case of, say, aggregated ethers and lactones, these numbers are determined by successive approximation. Naturally, chemical formulas $C_xH_yO_z(Imp)_{minor}$, constructed in this way and related to the same set of empirical chemical-content data, depend on the number of carbon atoms, i.e., on the size of graphene domains.

However, the presence of chemical formula does not allow for visualizing the BSU atomic structure. The problem is that a huge number of various-shaped graphene domains correspond to a given number of carbon atoms *x*. In its turn, a different number of edge atoms, subjected to targeting with heteroatoms, characterize shape-different domains. Moreover, the arrangement of heteroatoms over a set of the domain edge atoms is a difficult problem due to the large variability of multi-targeting, which is complicated by the high radicalization of these carbon atoms [145]. Therefore, in view of a practically infinite number of potential structural variations, none of the molecular structure of the $C_xH_yO_z(Imp)_{minor}$ chemical content, either drawn voluntarily by pen or designed by following particular algorithms, can take the place of an exact BSU view and is only one of a great number of possible 'snapshots'. Once so restricted with respect to real structures, the constructed BSUs are nevertheless useful, being the only structural images that allow for distinguishing the BSUs of different sp^2 aCs at the atomic level, immersing into the solids chemistry, exhibiting alive and silent chemical problems associated with the BSUs, disclosing the grounds and potentiality of different applications of sp^2 aCs, and so forth. Moreover, starting as molecular models of real solids, these virtual BSUs are easily transformed into Digital Twins [5,146] laying the foundation for reliable virtual analytics of the solids. Virtual vibrational spectrometry has so far been the first technique for the latter.

5.2. Molecular Models and Digital Twins of

BSUs of sp^2 Amorphous Carbons

In due course of the comprehensive analysis of the set of sp^2 aCs listed in Table 1 presented in the previous sections, a sufficient amount of data were obtained to enable the construction of BSUs models of the studied solids. Following general instructions, described in the previous section, rectangular graphene domains (5,5)NGr and (9,9)NGr with linear dimensions of 1.12×1.22 nm^2 and 1.97×2.20 nm^2, consisting of 66 and 190 carbon atoms, respectively, were chosen for modeling. According to the data in Table 2, the first domain is commensurate with the BSUs of natural solids and CB632, while the second is much bigger to be closer in size to the BSUs of CB624 and synthetic solids. Since the {CHO} triad evidently dominates in the chemical content in Table 3, we restricted ourselves with these elements only. Associated with the two domains mentioned above, the relevant BSU models listed in **Table 8** are presented in **Fig. 12***a–g*. We remind readers that the structures represent only instantaneous snapshots of numerous potential configurations of the same composition for each of the solids. It turned out that the analysis of numerical data on the chemical composition of BSUs from the viewpoint of XPS only is insufficient for a narrow choice of suitable structures [48]. It was necessary to plug DRIFT absorption spectra as well, which made it possible to significantly narrow the choice of structures to the set shown in the figure. A detailed discussion of building these models can be found in [49]. All structures are stable radicals [65] with temporarily quenched chemical activity. In the same way, BSU models can be built, which include, in addition to the triad of main components, minor impurities of nitrogen and sulfur [66] (see Fig. 12*h–j*). Evidently, these models, although not being exact imprints of the structure, make it possible to deal with sp^2 aCs with open eyes, understanding what the commonality and difference between natural amorphics are, and how the latter differ from synthetic and industrial ones. The difference in their behavior in catalysis [66], optics [147], medicine [148], etc. has the opportunity to become clearer.

Table 8

Chemical formulas of analytically provided models of basic structural units of sp^2 amorphous carbons.

No	Samples	Chemical formula
1	ShC	$C_{66}H_6O_4$
2	AnthX	$C_{66}H_{10}O_4$
3	AnthC	$C_{66}H_{14}O_4$
4	Ak-rGO	$C_{181}H_{27}O_{11}$
5	TE-rGO	$C_{185}H_{28}O_{19}$
6	CB632	$C_{66}H_2O_4$
7	CB624	$C_{181}O_9$

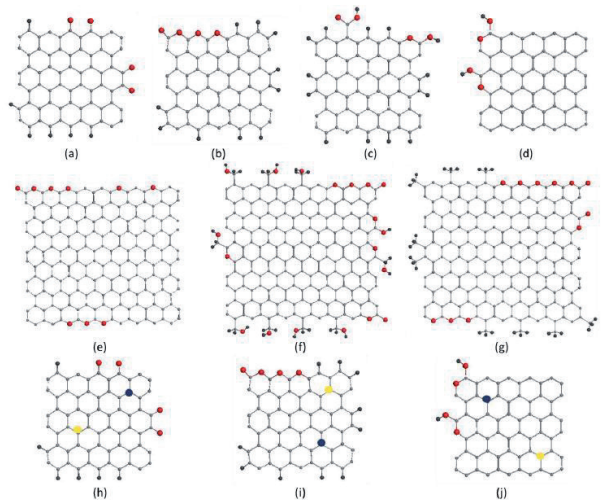

Fig. 12. *Molecular models of basic structure units of sp^2 amorphous carbons. Equilibrium structures of {CHO}-triad species: ShC (a), AnthX (b), AnthC (c), CB632 (d), CB624 (e), TE-rGO (f) and Ak-rGO (g). {CHO}-triad species complemented with nitrogen and sulfur additives: ShC (h), AnthX (i) and CB632 (j). Atomic content of the models follows the data listed in Table 3. Gray, red, black (a–g), completed with dark blue, yellow (h–j) balls depict carbon, hydrogen, oxygen, nitrogen and sulfur atoms, respectively.*

This first attempt at building empirically based models of NGMs opened up the possibility for a new direction of analytical research of sp^2 aCs aimed at moving from substances based on BSUs with an empirically unattainable structure, to those built from the NGMs of voluntary modified structure. Thus, going from individually different while not exactly determined empirical BSUs to a class of NGMs, undoubtedly having properties common to the whole class. This transition is possible within a new modeling concept known as the Digital Twins (DTs) [5,146]. The design of DTs is now subordinated not to the reproduction of the structure of empirical BSUs, but to respond to a series of questions aimed at elucidating one or another feature of the NGM class. In fact, when applied to a large set of NGMs [64,124,126], the approach has revealed many of the molecular commonalities, which are of practical interest, and which form the grounds of virtual

analytics of sp^2 aCs. First, this concerns virtual vibrational spectrometry that happened to be highly adaptive to a new analytic role.

5.3. Virtual Vibrational Analytics of sp² Amorphous Carbon

In molecular science the DT concept can be schematically presented as the following:

Digital twins → Virtual device → IT product.

This scheme connects three constituents of the approach [15]. Here, DTs are the molecular models under study, virtual device is a carrier of a selected software, and IT product covers a large set of computational results related to the DTs under different actions in the light of the soft explored. The quality of the IT product depends highly on how broadly and deeply the designed DTs cover all the knowledge concerning the object under consideration and how adequate the virtual device is to the peculiarities of this object. Applying virtual vibrational spectrometry, the virtual device is a virtual spectrometer. It should not contradict with the object nature and will perform calculations providing for the establishing of equilibrium structure of the designed DTs and obtaining their spectra of IR absorption and Raman scattering related to $3N–6$ vibrational modes. Virtual spectrometers differ by the software in grounds and are of HF (Hartree–Fock), DFT (density of functionals) or MD (molecular dynamics) type, since only semi-empirical programs based on the mentioned approximations can cope with the large volume of cumbersome calculations that are needed. As for quantum approaches, the radical nature of sp^2 aCs, caused by the open-shell electronic systems of their BSUs, forced us to abandon DFT- and MD-based softwares and pay particular attention to programs based on the unrestricted Hartree–Fock approximation. All the results illustrated below were obtained by using the virtual vibrational spectrometer HF Spectrodyn [149].

5.3.1. IINS Virtual Analytics

A standard model aimed at 'reading out' the empirical vibrational spectra of sp^2 aCs started far before the DT concept was introduced. The main problem preventing the issue from developing concerns the difficulty in building proper models. The situation changed appreciably when the first proposals to use NGMs as such models appeared. The models were initially applied for virtual IINS analytics of sp^2 aCs. Its main goal is to reproduce the solids behavior in the relevant empirical experiments. One-phonon GVDOS was the subject of calculations [87]. Two virtual experiments have been performed so far. The first mainly concerned adsorbed water in CB632, the empirical IINS spectrum of which is shown in Fig. 6*b*. A simplified BSU model, slightly different from the more detailed model that is shown in Fig. 12*d*, served as a carbon substrate immersed in the cloud of water molecules [2]. The second is related to a comparative analysis of empirical IINS spectra of sp^2 aCs presented in Fig. 9 using the first BSUs models, similar to those presented in Fig. 12 [47].

As seen in **Fig. 13**, the obtained virtual GVDOS is in line with the empirical data related to adsorbed water. In the second case, a set of virtual GVDOSs presented in **Fig 14** quite satisfactorily reproduced empirical data in the part related to the dependence of the spectra intensity on the hydrogen content of the relevant BSUs. Nearly linear dependence of the total spectrum intensity on the number of hydrogen atoms in the necklaces of the model BSUs was obtained [47], which follows the tendency of the hydrogen content of real sp^2 aCs listed in Table 3. A large width of the real IINS spectra does not allow for performing a more refined search of the BSUs models suitable for the spectra description [49].

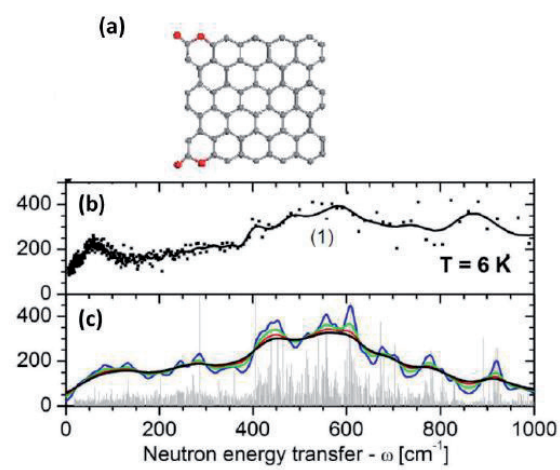

Fig. 13. *Adsorbed water in sp^2 amorphous carbon. (a) NGM model of BSUs of carbon blacks. (b) IINS-spectra-derived GVDOS of adsorbed water in as prepared CB632. (c) Virtual GVDOS of four-hydrogen-bond configured molecules of retained water. Gray and red balls depict carbon, and oxygen, respectively.*

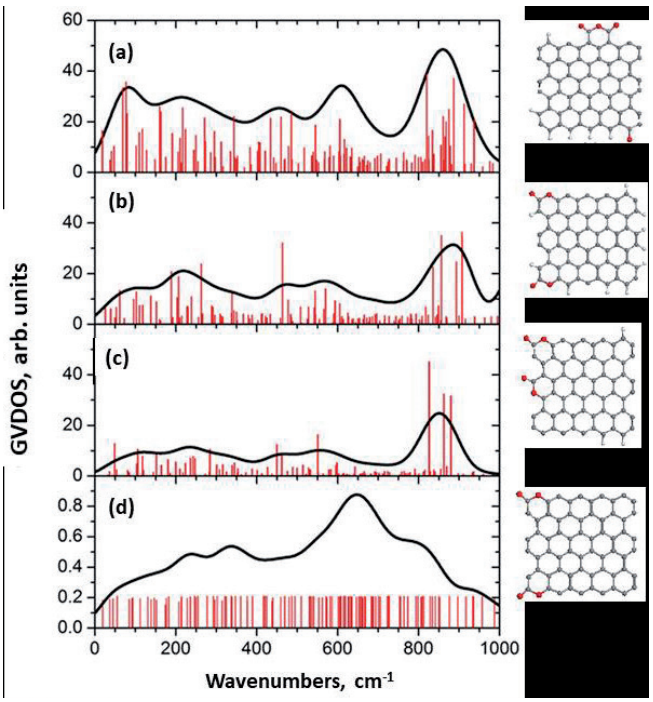

Fig. 14. *Virtual GVDOS spectra of graphene oxyhydrides related to the following BSUs' models: (a) ShC - $C_{68}O_4H_6$, (b) AnthX - $C_{64}O_4H_{10}$, (c) CB632 - $C_{64}O_4H_3$, and (d) CB624 - $C_{64}O_4$. Original bars are convoluted by Gaussian of 80 cm^{-1} half-width. Gray, white and red balls depict carbon, hydrogen and oxygen atoms, respectively.*

5.3.2. IR Absorption Virtual Analytics

The germination of virtual IR absorption analytics of sp^2 aCs has coincided with the beginning of transition of standard modeling of their individual molecular BSUs to the DT concept that concerns the class of NGMs [15,64,124,126]. A set of relatively reliable structural BSU models made it possible to penetrate their chemistry and begin to understand the main features of NGMs. In turn, the latter circumstance opened the way to recognize which information about molecules of this class can be obtained by asking the right questions. The latters should be formulated in the form of particular DT structures, whose treatment is aimed at receiving a clear answer to a particular inquiry. Referring the reader to the publications mentioned above for details, we confine ourselves to a brief enumeration of the answers received.

In terms of the DT concept, all the data discussed below were obtained using a virtual device-vibrational spectrometer HF Spectrodyn [149]. The obtained IT products present one-phonon harmonic spectra of IR absorption and Raman scattering. Their deviation from empirical analogues concerns the lack of anharmonicity and a considerable blue frequency shift. The former is highly important empirically, leading to a remarkable change in the optical spectra with respect to harmonic ones [150]. Nevertheless, the main features of both IR and Raman empirical spectra of the molecular sp2 nanocarbons are of harmonic origin. Accordingly, harmonic IT product reproduces the latter well enough. As for the unavoidable blue shift of virtual harmonic frequencies [151], it is quite considerable and constitutes ~200–500 cm^{-1} in the 1000–3500 cm^{-1} region. However, it is the same for all the studied DTs and can be ignored when comparing the virtual data of the species but should be taken into account at the final stage of comparing virtual and experimental data.

Digital Twins in place of real objects, and virtual spectrometers in place of real spectrometers, are real instruments of virtual vibrational spectrometry that provides the realization of many different goals. Comparative analysis, leading to the revealing of trends, common to both virtual and experimental spectra, is the strong point of the spectrometry. The unavoidable discrepancy of obtained individual virtual spectra and experimental data is its vulnerability. Obtaining the data presented below required consideration of several tens of DTs. Their design was carried out on the original graphene domains (5,5)NGr, (9,9)NGr, and (11,11)NGr. Digital Twins were conditionally divided into 'monochromic' and 'heterochromic' ones with respect to the chemical compositions of their necklaces. The former are carriers of highly distinguished identical chemical bonds while the latter are more adaptive to the varied chemical compositions of, say, empirical BSUs. Monochromic DTs with fully terminated edge atoms of the relevant graphene domains are of particular interest, presenting the effect of maximum contribution of the necklace heteroatoms into both the IR and Raman spectra of the molecules.

Fig. 15 presents a comparative view on the spectra of monochromic DTs based on the same graphene domain. As seen in the figure, the presence of heteroatoms drastically violates the DTs' IR spectra while leaving the Raman spectra practically unchanged. A thorough analysis of the data shown in the figure revealed that the following commonalities are inherent to all the NGMs, as well as to all of the sp^2 aCs BSUs.

1. Vibrational spectra of NGMs are determined by the pool of chemical bonds, among which sp^2C–C bonds configure graphene domains while sp^2C–A ones (A = H, O, N, S, and so forth) shape the NGMs' necklaces.
2. One-quantum harmonic vibration spectra of the NGMs, constituting of *N* atoms, cover 3*N*–*6* vibrational modes spread over the region of 0–1800 cm^{-1}, characterized for the excitation of sp^2C–C bonds, and of 0–3400 cm^{-1} depending on the sp^2C–A CBs configuration related to the NGM necklaces.
3. As seen in Fig. 15, all the NGMs' vibrational spectra contain a well-defined region of stretching vibrations of sp^2C–C bonds in the range of 1200–1800 cm^{-1} provided with the presence of graphene domains. The stretchings are slightly disturbed in Figure 15*c*–*e* due mainly to their reaction on the oxygen atoms presence in the NGMs' circumference (see detailed discussion of the feature in [124]).
4. The two communities of the NGMs' chemical bonds participate in their IR and Raman spectra quite differently. Covalent homopolar sp^2C–C bonds are not IR active due to a nil static dipole moment. Accordingly, IR absorption of graphene domains is extremely weak (Fig. 15*a*) while heteropolar sp^2C–A bonds show considerable absorption and are highly individually dependent on the chemical composition of the NGMs' necklaces (Fig. 15*b*–*e*). In contrast, activity of the Raman scattering is provided with sp^2C–C bonds in all the cases due to which the Raman signatures of bare graphene domains as well as NGMs are similar (Fig. 15*a*–*e*).
5. IR spectra, strongly dependent on the chemical composition of NGM necklaces, depend on the size of the latter rather weakly.
6. Analysis of virtual IR spectra of monochromic DTs allows for suggesting a definite set of group frequencies to be used for assignment of the spectra features to particular chemical bonds formed in the NGM necklaces.

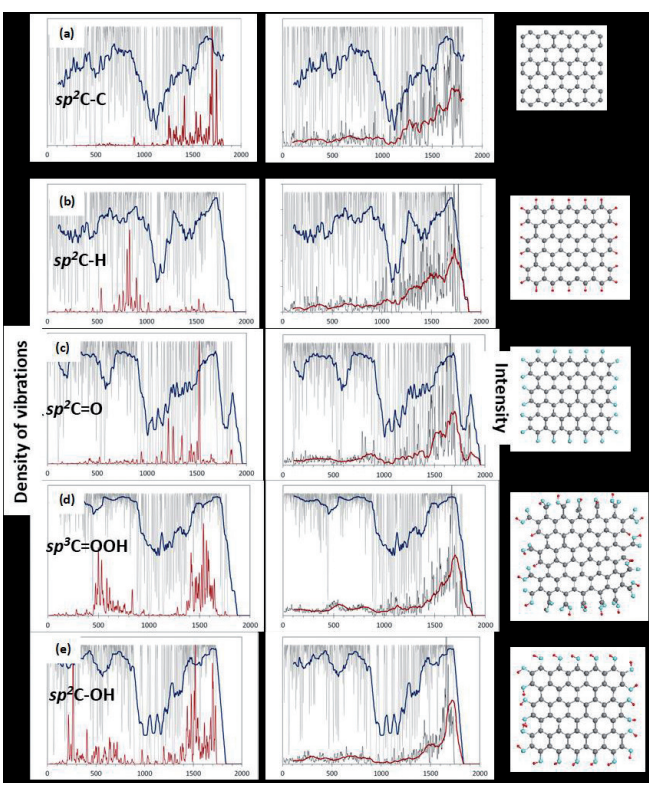

Fig. 15. *Virtual vibrational spectra (light gray) as well as one-phonon IR absorption and Raman scattering spectra (gray) of a set of the (5,5)NGr-based monochromic digital twins with fully terminated edge atoms of the graphene domains (a-e) [64]. Original sticks of the spectra are convoluted with Gaussian bandwidth of 10 cm^{-1}. Plottings of densities of vibrations and Raman spectra are accompanied with trend lines corresponding to 50–point linear filtration, dark blue and red, respectively. HF Spectrodyn virtual spectrometer. Equilibrium DT structures supplied with chemical formulas are presented on the right.*

In addition to exhibiting common trends of IR virtual spectrometry of NGMs discussed above, the first attempts were made to compare DTs' virtual spectra with the experimental ones of the relevant sp^2 aCs. Such a comparison related to TE-rGO is shown in **Fig. 16***a*. As seen in the figure, at first glance, the DRIFT spectrum of the object (red potting) differs drastically from the virtual one. However, once upshifted by 500 cm^{-1}, the three-band spectrum (blue plotting) correlates well with the similar three-band virtual one, reliably supporting the atomic configuration of the DT shown in the figure. Naturally, it is impossible to speak about the complete adequacy of the proposed model to the real BSU structure, but the fact of reproduction of the main components of the latter is obvious. Thus, the evidence, provided earlier with IINS as well as with DRIFT and XPS [49] spectra, is supported with virtual spectrometry.

A completely different situation is presented in Fig. 16*b*. In contrast to the previous case,

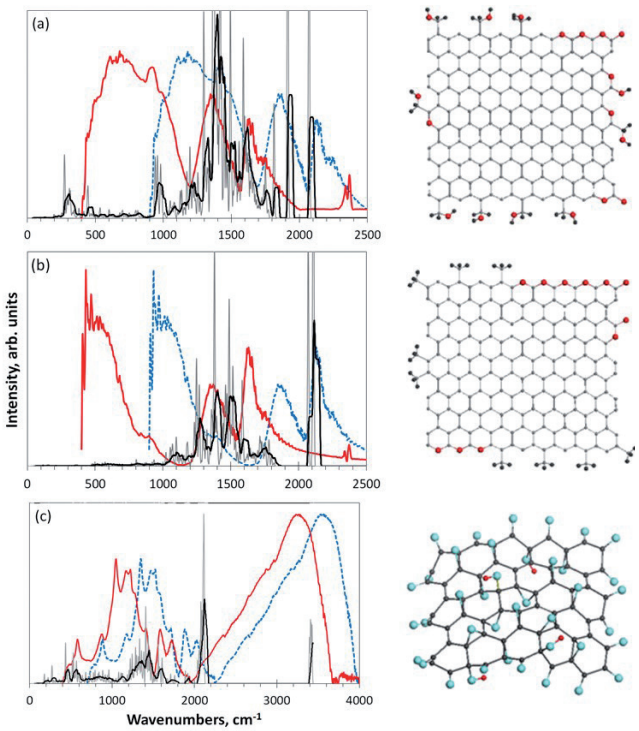

Fig. 16. *Digital twins' analytics of IR spectra of reduced and parental graphene oxides. (a,b) Virtual one-phonon (gray, supplemented with black trend lines corresponding to 50–point linear filtration, HF Spectrodyn) as well as original (red) and 500 cm^{-1} blue-shifted (blue) experimental IR absorption spectra of TE-rGO and Ak-rGO, respectively* [64]. *(c) The same but original and 300 cm^{-1} blue-shifted experimental IR spectra of graphene oxide* [124]. *Equilibrium structures of rGO's DTs $C_{185}H_{28}O_{19}$ and $C_{181}H_{27}O_{11}$ (see Table 8) as well as of GO's DT $C_{66}O_{40}H_4$ are shown on the right.*

the experimental spectrum of Ak-rGO, which deviates significantly from that for TE-rGO, is different from the virtual spectrum of DT as well. As can be seen, a similar upshift does not reveal any similarity between the real and virtual spectra, except for the band at ~1700 cm^{-1}. This band is perhaps the only evidence of the presence of quinones in the structure of both real Ak-rGO BSU and DT. As for the low-frequency part of the real spectrum in the region of 500–800 cm^{-1}, analysis of virtual spectra of monochromic DTs in Fig. 15 as well as many others point to its attribution to hydrogen atoms in the nearest vicinity to edge atoms of the NGMs' graphene domains. Such atoms are not presented in the DT chemical structure, which might explain the drastic discrepancy between the empirical and virtual IR spectra. As for reality, adsorbed water is the first candidate to be examined. Obviously, the presence of this water in TE-rGO may improve the fit between the empirical and virtual spectra in this region as well. The DT concept, worked out by example of NGMs [64,126], has recently been applied to the graphene oxide IR spectrum [124], positive result of which is shown in Fig. 16*c*.

5.3.3. Raman Scattering Virtual Analytics

The main features of NGMs' Raman spectra are presented in **Fig. 17** in a compressed way. The Digital Twins' analytics of Raman scattering spectra of NGMs [64,126] has revealed the following commonalities:

1. As evidenced in Figs 15 and 17, the graphene domain sp^2C-C stretchings determine the main pattern of the NGMs' Raman spectra.
2. The Raman spectra of NGMs respond to the presence of heteroatoms in the molecules' circumference due to the frequency difference of the sp^2C–C and sp^2C–C(A) stretchings [124] (see Fig. 15). However, the violation is not critical to significantly disturb the general similarity of the

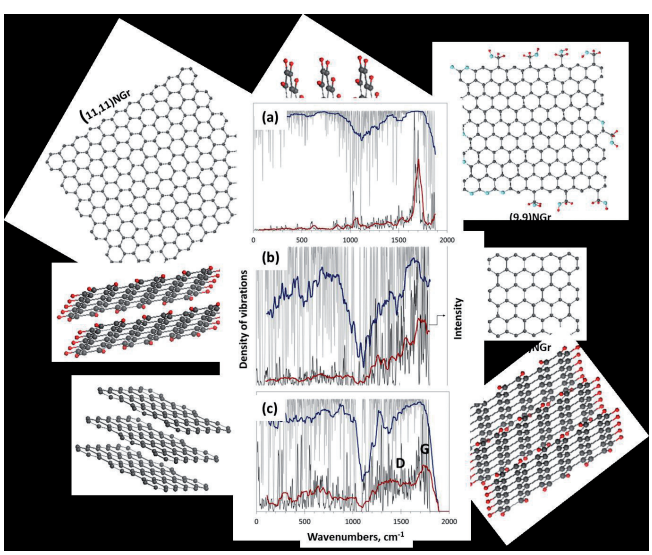

Fig. 17. *Digital twins' analytics of Raman spectra of individual and layered NGMs of different size and compositions. (a,b). Virtual densities of vibrations (light gray) and one-phonon Raman spectra (gray) of one-layer TE-rGO ($C_{192}O_{19}H_{44}$) and bare domain (5,5) NGr (C_{66}), respectively. (c) The same but two layers of hydrogenated domain (5, 5) NGr ($C_{132}H_{44}$). Original sticks of the spectra are convoluted with Gaussian bandwidth of 10 cm^{-1}. Both densities of vibrations and Raman spectra are accompanied with 50-points trend lines, dark blue and red, respectively. HF Spectrodyn. Adapted from Refs.* [64,126].

Raman spectra appearance of the different sp^2 aCs presented in Fig. 11.

3. The Raman spectra of individual NGMs of any chemical composition are not characterized with a standard *D*–*G* doublet as seen in Figs 15.
4. The Raman spectra of individual NGMs strongly depend on their linear dimensions and are transformed from a broad-band (see Fig. 17*b*) to narrow-band with a total domination of G-band when the size of the latter approaches the free path of graphene optical phonons L_{ph} ~15 nm [143] (see Fig 17*a*). The effect, which is typical size effect of phonon spectra of molecular amorphous solids [152], strengthens when (9,9) graphene domain is substituted with (11,11) [64].
5. The appearance of the *D*-band and formation of the *D*–*G* doublet is a particular feature attributed to NGM layering (see Fig. 17*c*). The effect becomes more pronounced when a double layer NGM is substituted with a three-layer one [64]. It is provided with the generation of dynamically stimulated sp^3C–C bonds between the carbon atoms of adjacent NGM layers [124] due to the exact van der Waals contact between them. A high activity of out-of-plane stretchings of benzenoid units [116,137] makes the sp3C–C stretchings active enough to generate the D-band.
6. The D-band's intensity increases when the number of NGM layers grows up to 4–5 nm and then markedly slows down when the stack thickness exceeds ~15 nm [142].

6. EXPRESS ANALYSIS OF SP^2 AMORPHOUS CARBONS BASED ON IR AND RAMAN SPECTRA

Evidently, all the above concerns the Raman spectra of real sp^2 aCs, particularly, the solids' short-range order presented with the relevant BSUs and their stacks and can be applied for analysis of empirical spectra of the solids, in general, and for their express analysis, in particular. Results of the latter, applied to a randomly selected sample [153], are demonstrated in **Fig. 18**. Starting from the Raman spectrum in Fig. 18*a*, one has to be convinced first in dealing with a sp^2 aC, but not with graphene oxide, whose Raman spectrum looks exactly as shown in the figure [124]. Convinced by the XRPD test, we move on to read out the Raman spectrum of the rGO solid. It tells us that the solid has a stacked structure consisting of 4–5 BSUs layers, BSUs linear size being its first nanometers. A considerable width of *D*- and *G*-bands allows for suspecting a turbostratic nature of the layer packaging. Evidently, the presence of the BSUs' necklaces is one of the reasons for both this disordering and slight increasing of the interlayer distance, as shown in Table 2. In its turn, the IR absorption spectrum in Fig. 18*b* shows that this rGO's necklace is mainly oxygenated, since none of the prominent sp^2C–H models, which are concentrated below 1000 cm^{-1}, are revealed. No traces of adsorbed water (region below 400 cm^{-1}) are fixed as well. Following the group frequencies listed in Table 7, it is possible to suggest the oxygen-containing contributions indicated in the figure. A rather scares fine structure of the IR spectrum is in line with the attribution of marked bands below 2000 cm^{-1} to cyclic ethers, while the band at 3400 cm^{-1} evidences traces of small amount of hydroxyls in the sample. The presented express analysis of the Raman and IR absorption spectra of an rGO sample is only the beginning of the in-depth analysis and is given as an example. Nevertheless, it provides a reliable entry level of analysis requiring further confirmation using all the advanced methods of analytical chemistry and spectroscopy.

7. CONCLUSIVE REMARKS

The first atlas of empirical and virtual analytics of sp^2 amorphous carbons is over. It opens the way

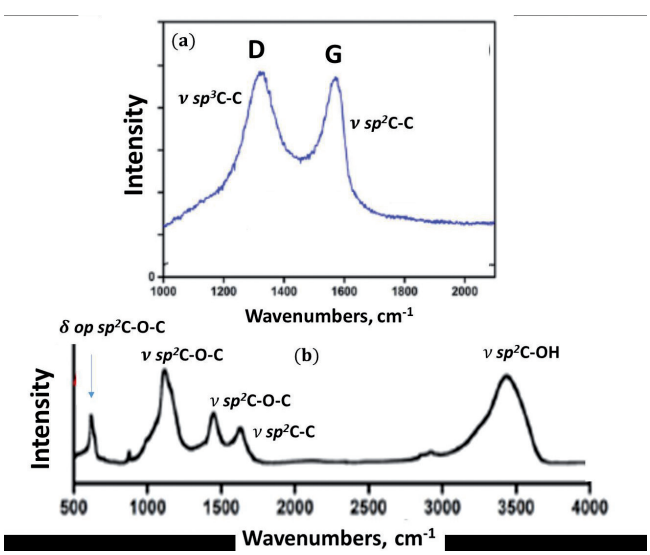

Fig. 18. *Express analysis of sp^2 amorphous carbon. Raman scattering (a) and IR absorption (b) spectra of a lab-fabricated reduced graphene oxide [153] in notations of vibrational analytics (see text).*

for further development, extension, sophistication, routing, substitution and suggests new visions and approaches. Both analytics are based on the molecular nature of the solids and are aimed at the disclosure and characterization of short-range order of the latter. The two analytics are not perfect and there are still questions to be raised and answered. What is presented for the reader's judgment is only the first attempt to summarize the currently available ideas about sp^2 amorphous carbon and offer a systematic way to check and analyze them.

Funding: This research receives no external funding.

Institutional Review Board Statement: Not applicable.

Informed Consent Statement: Not applicable.

Data Availability Statement: Any data or material that support the findings of this study can be made available by the corresponding author upon request.

Conflicts of Interest: The author declares no conflict of interests.

List of abbreviations

aC amorphous carbon
AFM atom-force microscopy
Ak-rGO lab rGO product
AnthC anthracite
AnthX anthraxolite
BSU basic structural unit
CB carbon black
DFT density functional theory
DRIFT Diffused-reflection IT Fourier determined spectrometer
DT digital ywin
DTA differential thermal analysis
DSC differential scanning calorimetry
EDS energy dispersion spectroscopy
EA elemental analysis
EM electron microscopy
FTIR Fourier determined IR spectroscopy
FWHM full width at half maximum
GBE group bending energy
GF group frequency
GO graphene oxide
GVDOS generalized vibrational density of states
HF Hartree-Fock approximation
HREELS high-resolution electron energy loss spectroscopy
HRTEM high-resolution transmission electron microscopy
IINS inelastic incoherent neutron spectroscopy
IT intellectual technology
MD molecular dynamics
NGM necklaced graphene molecule
NPD neutron powder diffraction
PD powder diffraction
rGO reduce graphene oxide
SEM scanning electron microscopy
ShC shungite carbon
STEM scanning transmission electron microscopy
TE-rGO thermally exfoliated rGO
VFF Voigt fitting function
XRPD X-ray powder diffraction
XPS X-ray photoelectron spectroscopy

REFERENCES

1. Sheka, E.F.; Rozhkova, N.N. Shungite as the natural pantry of nanoscale reduced graphene oxide. *Int. J. Smart Nano Mat.,* 2014, 5:1-16.
2. Hoffmann, R. Small but strong lessons from chemistry for nanoscience. *Angew. Chem. Int. Ed.*, 2013, 52:93-103.
3. Elliot, S.R. *Physics of Amorphous Materials.* Longman: London, UK; New York, NY, USA, 1983.
4. Raman, C.V. Molecular structure of amorphous solids. *Nature,* 1922, 109:138-139.
5. Natkaniec, I.; Sheka, E.F.; Drużbicki, K.; Hołderna-Natkaniec, K.; Gubin, S.P.; Buslaeva, E.Y.; Tkachev, S.V. Computationally Supported Neutron Scattering Study of Parent and Chemically Reduced Graphene Oxide. *J. Phys. Chem. C*, 2015, 119:18650-18662.
6. Donet, J.-B.; Bansal, R.C.; Wang, M.-J. (Eds.). *Carbon Black. Science and Technology.* Marcel Dekker: New York, NY, USA; Basel, Switzerland, 1993.
7. Rozhkova, N.N.; Rozhkov, S.P.; Goryunov, A.S. Natural graphene-based shungite nanocarbon. In: *Carbon Nanomaterials Sourcebook*; Sattler, K.D., Ed.; CRC Press: Roca Raton, FL, USA; London, UK; New York, NY, USA, 2016; Volume 1, pp. 151-174.
8. Filippov, M.M. *Anthraxolites*. VNIGRI: St. Petersburg, Russia, 2013, (in Russ.).
9. Skripchenko, G.B. Structure, properties and use of anthracytes of the Donetsk basin. *Chem. Solid Fuel,* 2010, 2:3-13, (in Russ.).
10. Tkachev, S.V.; Buslaeva, E.Y.; Naumkin, A.V.; Kotova, S.L.; Laure, S.V.; Gubin, S.P. Reduced graphene oxide. *Inorg. Mat.*, 2012, 48:796-802.
11. Sheka, E.F.; Natkaniec, I.; Mel'nikov, V.; Druzbicki, K. Neutron scattering from graphene oxide paper and thermally exfoliated reduced graphene oxide. Nanosyst. Phys. Chem. Math. 2015, 6, 378–393.
12. SIGMA-ALDRICH. Synthesis of mesoporous materials. *Mat. Matt*, 2008, 3:17-18.
13. Sheka, E.F.; Golubev, E.A. Technical graphene (reduced graphene oxide) and its natural analog (schungite). *Tech. Phys.*, 2016, 61:1032-1038.

14. Sheka, E.F. Digital Twins in the graphene technology. *arXiv 2022*, https://doi.org/10.48550/arXiv.2208.14926.
15. Radovic, L. (Ed.). *Chemistry and Physics of Carbon*. Marcel Dekker: New York, NY, USA, 2001.
16. Setton, R.; Bernier, P.; Lefrant, S. (Eds.). *Carbon Molecules and Materials*. Taylor and Francis: London, UK; New York, NY, USA, 2002.
17. Filippov, M.M. *Shungite-Bearing Rocks of the Onega Structure*. Karelian Science Centre of RAS: Petrozavodsk, Russia, 2002, (in Russ.).
18. Silva, R.; Silva, S.R.P. (Eds.). *Properties of Amorphous Carbon*. INSPEC: London, UK, 2003.
19. Marsh, H.; Rodriguez-Reinoso, F. (Eds.). *Activated Carbon*. Elsevier Science & Technology Books: Amsterdam, The Netherlands, 2006.
20. Gogotsi, Y. (Ed.). *Carbon Nanomaterials*. Taylor and Francis Group, LLC: Boca Raton, FL, USA, 2006.
21. Radovic, L. (Ed.). *Chemistry and Physics of Carbon*. Taylor and Francis Group, CRC Press: Boca Raton, FL, USA, 2008.
22. Serp, P.; Figueiredo, J.L. (Eds.). *Carbon Materials for Catalysis*. Wiley: Hoboken, NJ, USA, 2009.
23. Colombo, L.; Fasolino, A. (Eds.). *Computer-Based Modeling of Novel Carbon Systems and Their Properties, Carbon Materials: Chemistry and Physics 3*. Springer Science + Business Media B.V.: Berlin/Heidelberg, Germany, 2010.
24. Oberlin, A.; Bonnamy, S. A realistic approach to disordered carbons. In: *Chemistry and Physics of Carbon*. Radovic, L., Ed.; CRC Press: Boca Raton, FL, USA, 2013.
25. Serp, P.; Machado, B. (Eds.). *Nanostructured Carbon Materials for Catalysis*. RSC: Croydon, UK, 2015.
26. Putz, M.V.; Ori, O. (Eds.). *Exotic Properties of Carbon Nanomatter. Advances in Physics and Chemistry. Carbon Materials: Chemistry and Physics*. Springer Science + Business Media: Dordtrecht, The Netherlands, 2015.
27. Sattler, K.D. (Ed.). *Carbon Nanomaterials Sourcebook*. CRS Press: Boca Raton, FL, USA; London, UK; New York, NY, USA, 2016.
28. Sheka, E. *Spin Chemical Physics of Graphene*. Pan Stanford: Singapore, 2018.
29. Kharisov, B.I.; Kharissova, O.V. *Carbon Allotropes: Metal-Complex Chemistry, Properties and Applications*. Springer Nature: Cham, Switzerland, 2019.
30. Ray, S.C. *Magnetism and Spintronics in Carbon and Carbon Nanostructured Materials*. Elsevier: Dodrecht, The Netherlands, 2020.
31. Borghi, F.; Soavi, F.; Milani, P. (Eds.). *Nanoporous Carbons for Soft and Flexible Energy Devices. Carbon Materials: Chemistry and Physics*. Springer Nature: Cham, Switzerland, 2022.
32. Uspensky, V.A.; Radchenko, O.A.; Glebovskaya, E.A. *Basics of Genetic Classification of Bitumen*. USSR, Leningrad, Nedra Publ., 1964, (in Russ.).
33. Cornelius, C.D. Classification of natural bitumen: A physical and chemical approach. In: *Exploration for Heavy Crude Oil Fnd Natural Bitumen*. Meyer, R.F., Ed.; AAPG Studies in Geology: Tulsa, OK, USA, 1987; Volume 25, pp. 165–174.
34. Jakob, H. Nomenclature, classification, characterization and genesis of natural solid bitumen (Migrabitumen). In: *Bitumen in Ore Deposits*. Parnell, J., Kucha, H., Landais, P., Eds.; Springer: Berlin/Heidelberg, Germany, 1993; pp. 11-27.
35. Mossman, D.J.; Nagy, B. Solid bitumens: An assessment of their characteristic, genesis, and role in geological processes. *Terra Nova,* 1996, 8:114-128.
36. Sheka, E.F.; Golubev, Y.A.; Popova, N.A. Amorphous state of sp^2 solid carbon. FNCN, 2021, 29:107-113.
37. Shumilova, T.G. *Mineralogy of Native Carbon*. Ural Dept RAS: Yekaterinburg, Russia, 2003, (in Russ.).
38. Shumilova, T.G.; Isaenko, S.I.; Divaev, F.K. Mineralogical features of diamond, amorphous diamond like carbon and graphite from Chagatay carbonatites (Uzbekistan). *Mineral. J.,* (Ukr.) 2013, 35:81-89.
39. Robertson, J. Diamond-like amorphous carbon. *Mater. Sci. Eng. R Rep.*, 2002, 37:129-281.
40. Zhang, L.; Wei, X.; Lin, Y.; Wang, F. A ternary phase diagram for amorphous carbon. *Carbon*, 2015, 94:202-213.
41. Harris, P.J.F. New perspectives on the structure of graphitic carbons. *Crit. Rev. Solid State Mat. Sci.*, 2005, 30:235-253.
42. Chua, C.K.; Pumera, M. Chemical reduction of graphene oxide: A synthetic chemistry viewpoint. *Chem. Soc. Rev.,* 2014, 43:291-312.
43. Krishnan, D.; Kim, F.; Luo, J.; Cruz-Silva, R.; Cote, L.J.; Jang, H.D.; Huang, J. Energetic

graphene oxide: Challenges and opportunities. *Nanotoday*, 2012, 7:137-152.
44. Chyan, Y.; Ye, R.; Li, Y.; Singh, S.P.; Arnusch, C.J.; Tour, J.M. Laser-induced graphene by multiple lasing: Toward electronics on cloth, paper, and food. *ACS Nano*, 2018, 12:2176-2183.
45. Luong, D.X.; Bets, K.V.; Algozeeb, W.A.; Stanford, M.G.; Kittrell, C.; Chen, W.; Salvatierra, R.V.; Ren, M.; McHugh, E.A.; Advincula, P.A.; et al. Gram-scale bottom-up flash graphene synthesis. *Nature*, 2020, 577:647-651.
46. Seal, M. The effect of surface orientation on the graphitization of diamond. *Phis. Stat. Sol.*, 1963, 3:658.
47. Sheka, E.F.; Hołderna-Natkaniec, K.; Natkaniec, I.; Krawczyk, J.X.; Golubev, Y.A.; Rozhkova, N.N.; Kim, V.V.; Popova, N.A.; Popova, V.A. Computationally supported neutron scattering study of natural and synthetic amorphous carbons. *J. Phys. Chem. C*, 2019, 123:15841-15850.
48. Golubev, Y.A.; Rozhkova, N.N.; Kabachkov, E.N.; Shul'ga, Y.M.; Natkaniec-Hołderna, K.; Natkaniec, I.; Antonets, I.V.; Makeev, B.A.; Popova, N.A.; Popova, V.A.; Sheka, E.F. sp^2 Amorphous carbons in view of multianalytical consideration: Normal, expected and new. *J. Non-Cryst. Solids,* 2019, 524:119608.
49. Sheka, E.F.; Natkaniec, I.; Ipatova, E.U.; Golubev, Y.A.; Kabachkov, E.N.; Popova, V.A. Heteroatom necklaces of sp^2 amorphous carbons. XPS supported INS and DRIFT spectroscopy. FNCN, 2020, 28:1010-1029; https://doi.org/10.1080/1536383X.2020.1794849.
50. Sheka, E.F.; Golubev, Y.A.; Popova, N.A. Graphene domain signature of Raman spectra of sp2 amorphous carbons. *Nanomaterials*, 2020, 10:2021.
51. Razbirin, B.S.; Rozhkova, N.N.; Sheka, E.F.; Nelson, D.K.; Starukhin, A.N. Fractals of graphene quantum dots in photoluminescence of shungite. *J. Exp. Theor. Phys.*, 2014, 5:838-850.
52. Avdeev, M.V.; Tropin, T.V.; Aksenov, V.L.; Rosta, L.; Garamus, V.M.; Rozhkova, N.N. Pore structures in shungites as revealed by small-angle neutron scattering. *Carbon*, 2006, 44:954-961.
53. Broude, V.L.; Klimusheva, G.V.; Prikhotjko, A.F.; Sheka, E.F.; Yatcenko, L.P. *Absorption Spectra of Molecular Crystals*. Polysubstituted Benzene Compounds; Naukova Dumka: Kiev, USSR, 1972, (in Russ.).
54. Sheka, E.F. Spectroscopy of amorphous substances with molecular structure. *Sov. Phys. Usp.*, 1990, 33:147-166.
55. Golubev, Y.A.; Ulyashev, V.V.; Veligzhanin, A.A. Porosity and structural parameters of Karelian shungites according to the data of small-angle synchrotron radiation scattering and microscopy. *Crystallgr. Rep.,* 2016, 61:66-77.
56. Rozhkova, N.N. Aggregation and stabilization of shungite carbon nanoparticles. *Ecol. Chem.*, 2012, 4:240-251.
57. Duan, X.; Ao, Z.; Zhang, H.; Saunders, M.; Sun, H.; Shao, Z.; Wang, S. Nanodiamonds in sp2 /sp3 configuration for radical to nonradical oxidation: Core-shell layer dependence. *Appl. Cat. B: Envirom.*, 2018, 222:176-181.
58. Sadovnichii, R.V.; Rozhkov, S.S.; Rozhkova, N.N. The use of shungite processing products in nanotechnology: Geological and Mineralogical Justification. *Smart Nanocomp.*, 2016, 7:111-119.
59. Garvie, L.A.J.; Buseck, P.R. Carbonaceous materials in the acid residue from the Orgueil carbonaceous chondrite meteorite. *Meteor. Planet. Sci.*, 2006, 41:633-642.
60. Taskaev, S.; Skokov, K.; Khovaylo, V.; Donner, W.; Faske, T.; Dudorov, A.; Gorkavyi, N.; Muratov, D.S.; Savosteenko, G.; Dyakonov, A.; et al. Exotic carbon microcrystals in meteoritic dust of the Chelyabinsk superbolide: Experimental investigations and theoretical scenarios of their formation. *Eur. Phys. J. Plus,* 2022, 137:562.
61. Povarennykh, M.Y.; Matvienko, E.N.; Knot.ko, A.V.; Shatalova, T.B. Characteristic of natural carbon nanominerals and their aggregates from the Dzhaharduk area (Uzbekistan). *Mineral,* 2018, 4:85-97.
62. Allen, K.D.; Wegener, G.; Matthew Sublett, D., Jr.; Bodnar, R.J.; Feng, X.; Wendt, J.; White, R.H. Biogenic formation of amorphous carbon by anaerobic methanotrophs and select methanogens. *Sci. Adv.*, 2021, 7:eabg9739.
63. Melezhik, V.A.; Filippov, M.M.; Romashkin, A.E. A giant Palaeoproterozoic deposit of shungite in NW Russia: Genesis and practical applications. *Ore Geol. Rev.*, 2004, 24:135-154.

64. Sheka, E.F.; Popova, N.A. Virtual vibrational analytics of reduced graphene oxide. *Int. J. Mol. Sci.*, 2022, 23:6978.
65. Sheka, E.F. sp2 Carbon stable radicals. C 2021, 7, 31.
66. Deng, D.; Yu, L.; Pan, X.; Wang, S.; Chen, X.; Hu, P.; Sunb, L.; Bao, X. Size effect of graphene on electrocatalytic activation of oxygen. *Chem. Commun.*, 2011, 47:10016-10018.
67. Sheka, E.F. Graphene oxyhydride catalysts in view of spin radical chemistry. *Materials,* 2020, 13:565.
68. Jurkiewicz, K.; Pawlyta, M.; Burian, A. Structure of carbon materials explored by local transmission electron microscopy and global powder diffraction probes. *Carbon*, 2018, 4:68.
69. Warren, B.E. X-ray diffraction in random layer lattices. *Phys. Rev.*, 1941, 59:693-698.
70. Biscoe, J.; Warren, B.E. An X-ray study of carbon black. *J. Appl. Phys.*, 1942, 13:364-371.
71. Busek, P.R.; Galdobina, I.P.; Kovalevski, V.V.; Rozhkova, N.N.; Valley, J.W.; Zaidenberg, A.Z. Shungites: The C-rich rocks of Karelia, Russia. *Can. Mineralog.*, 1997, 35:1363-1378.
72. Kovalevskii, V.V. The Structure of Carbon Matter and the Genesis of Shungite Rocks. *Dr. Sci. Dissertation, Geology and Mineralogy*, Petrozavodsk, Russia, 2007.
73. Golubev, E.A. Globular structure of higher anthraxolites according to scanning probe microscopy. *Dokl. Ak. Nauk.*, 2009, 425:519-521, (in Russ.).
74. Golubev, E.A. Electrophysical properties and structural features of shungite. *Phys. Solid State,* 2013, 55:1078.
75. Available online: http//rsb.info.nih.gov/ij (accessed on).
76. Osváth, Z.; Deák, A.; Kertész, K.; Molnár, G.; Vértesy, G.; Zámbó, D.; Hwang, C.; Biró, L.P. The structure and properties of graphene on gold nanoparticles. *Nanoscale*, 2015, 7:5503-5509.
77. Klug, H.P.; Alexander, L.E. X-Ray *Diffraction Procedures for Polycrystalline and Amorphous Materials*, 2nd Ed.; John Wiley: New York, NY, USA, 1974.
78. Ingham, B. X-ray scattering characterization of nanoparticles. *Cryst. Rev.,* 2015, 21:229-303.
79. Kisi, E.H.; Howard, C.J. *Applications of Neutron Powder Diffraction.* Oxford University Press: New York, NY, USA, 2008; 384 p.
80. Sheka, E.F.; Rozhkova, N.N.; Holderna-Natkaniec, K.; Natkaniec, I. Nanoscale reduced-graphene-oxide origin of shungite in light of neutron scattering. *Nanosyst. Phys. Chem. Math.*, 2014, 5:659-676.
81. Lobzova, R.V. *Graphite and Alkaline Rocks of the Botogol'sk Massif.* Moscow, Nauka Publ., 1975, (in Russ.).
82. Langford, J.I.; Wilson, A.J.C. Scherrer after sixty years: A survey and some new results in the determination of crystallite size. *J. Appl. Cryst.,* 1978, 11:102-113.
83. Vorokh, A.S. Scherrer formula: Estimation of error in determining small nanoparticle size. *Nanosyst. Phys. Chem. Mat.*, 2018, 9:364-369.
84. Sofer, Z.; Šimek, P.; Jankovsky, O.; Sedmidubsky, D.; Beran, P.; Pumera, M. Neutron diffraction as a precise and reliable method for obtaining structural properties of bulk quantities of graphene. *Nanoscale*, 2014, 6:13082-13089.
85. Opalev, S.V.; Belenkov, E.A. Experimental study of graphites structure change under mechanical grinding. *Bull. Chelyabinsk. Sci. Cent.*, 2004, 3:27-30. (in Russ.).
86. Klancnik, G.; Medved, J.; Mrvar, P. Differential thermal analysis (DTA) and differential scanning calorimetry (DSC) as a method of material investigation. *RMZ Mat. Geoenv.*, 2010, 57:127-142.
87. Mitchel, P.C.H.; Parker, S.F.; Ramirez-Cuesta, A.J.; Tomkinson, J. Vibrational Spectroscopy with Neutrons. In: *With Application in Chemistry, Biology, Materials Science and Catalysis.* World Scientific: Singapore, 2005.
88. Huang, H.; Sun, G.; Hu, J.; Jiao, T. Low temperature synthesis of MnO2/graphene nanocomposites for supercapacitors. *J. Chem.,* 2015, 2015, 629362.
89. Goldstein, J.; Newbury, D.E.; Echlin, P.; Joy, D.C.; Romig, A.D.; Lyman, C.E. Scanning Electron Microscopy and X-Ray Microanalysis. In: *A Text for Biologists, Materials Scientists, and Geologists*, 2nd Ed.; Plenum Press: New York, NY, USA, 1992.
90. CasaXPS User's Manual; Casa Software Ltd.: San Diego, CA, USA, 2001.
91. Plyusnina, L.P.; Likhoidov, G.G.; Kuzmina, T.V. Graphitization and naphthide-ore genesis. *Litosphere*, 2011, 5:111-116. (in Russ.).

92. Shumilova, T.G.; Shevchuk, S.S.; Isayenko, S.I. Metal concentrations and carbonaceous matter in the black shale type rocks of the Urals. *Dokl. Earth Sci.,* 2016, 469:695-698.
93. Moldoveanu, S.C. *Pyrolysis of Organic Molecules with Application to Health and Enviromental Issues*, 2nd ed. Elsevier: Amsterdam, The Netherlands, 2018.
94. Darmstadt, H.; Roy, C.; Kaliaguine, S. ESCA characterization of commercial carbon blacks and of carbon blacks from vacuum pyrolysis of used tires. *Carbon*, 1994, 32:1399-1406.
95. Cheng, C.-H.; Lehmann, J.; Thies, J.E.; Burton, S.D.; Engelhard, M.H. Oxidation of black carbon by biotic and abiotic processes. *Org. Geochem.*, 2006, 37:1477-1488.
96. Shao, Y.; Yin, G.; Zhang, J.; Gao, Y. Comparative investigation of the resistance to electrochemical oxidation of carbon black and carbon nanotubes in aqueous sulfuric acid solution. Electrochim. Acta 2006, 51, 5853–5857.
97. Nikitin, A.; Li, X.; Zhang, Z.; Ogasawara, H.; Dai, H.; Nilsson, A. Hydrogen storage in carbon nanotubes through the formation of stable C−H bonds. *Nano Lett.,* 2008, 8:162-167.
98. Yan, J.; Wei, T.; Shao, B.; Ma, F.; Fan, Z.; Zhang, M.; Zheng, C.; Shang, Y.; Qian, W.; Wei, F. Electrochemical properties of graphene nanosheet/carbon black composites as electrodes for supercapacitors. *Carbon*, 2010, 48:1731-1737.
99. Schuster, M.E.; Havecker, M.; Arrigo, R.; Blume, R.; Knauer, M.; Ivleva, N.P.; Su, D.S.; Niessner, R.; Schlogl, R. Surface sensitive study to determine the reactivity of soot with the focus on the European emission standards IV and VI. *J. Phys. Chem. A,* 2011, 115:2568-2580.
100. Chen, W.; Zhu, Z.; Li, S.; Chen, C.; Yan, L. Efficient preparation of highly hydrogenated graphene and its application as a high-performance anode material for lithium ion batteries. *Nanoscale*, 2012, 4:2124-2129.
101. Kalazhokov, Z.K.; Naumkin, A.V.; Zhansitov, A.;, Khashirova, S.Yu.; Kalazhokov, K.H.; Karamurzov, B.S. Investigation of carbon fiber/polyphenylenesulfone composites by method of X-ray photoelectron spectroscopy. *Key Engin. Mat.*, 2019, 816:37-42.
102. Komarova, N.S.; Krivenko, A.G.; Ryabenko, A.G.; Naumkin A.V. Active forms of oxygen as agents for electrochemical functionalization of SWCNTs. *Carbon,* 2013, 53:188-196.
103. Wang, J.; Chen, Z.; Chen, B. Adsorption of polycyclic aromatic hydrocarbons by graphene and graphene oxide nanosheets. *Environ. Sci. Technol.*, 2014, 48:4817-4825.
104. Gusmjo, R.; Sofer, Z.; Bouša, D.; Pumera, M. Synergetic metals on carbocatalyst shungite. *Chem. Eur. J.*, 2017, 23:18232-18238.
105. Beamson, G.; Briggs, D. High Resolution XPS of Organic Polymers. In: *The Scienta ESCA300 Database.* Wiley: Chichester, UK, 1992.
106. Acik, M.; Lee, G.; Mattevi, C.; Chhowalla, M.; Cho, K.; Chabal, Y.J. Unusual infrared-absorption mechanism in thermally reduced graphene oxide. *Nat. Mater.,* 2010, 9:840-845.
107. Acik, M.; Lee, G.; Mattevi, C.; Pirkle, A.; Wallace, R.M.; Chhowalla, M.; Cho, K.; Chabal, Y. The role of oxygen during thermal reduction of graphene oxide studied by infrared absorption spectroscopy. *J. Phys. Chem. C,* 2011, 115:19761-19781.
108. Kim, S.; Zhou, S.; Hu, Y.; Acik, M.; Chabal, Y.J.; Berger, C.; De Heer, W.; Bongiorno, A.; Riedo, E. Room-temperature metastability of multilayer graphene oxide films. *Nat. Mater.*, 2012, 11:544-549.
109. Radovich, L.R.; Bockrath, B. On the chemical nature of graphene edges: origin of stability and potential for magnetism in carbon materials. *JACS,* 2005, 127:5917-5927.
110. Serp, P.; Machado, B. (Eds.). *Nanostructured Carbon Materials for Catalysis*. Royal Society of Chemistry: Croydon, UK, 2015.
111. Villa, A.; Dimitratos, N. (Eds.) *Metal-free Functionalized Carbons in Catalysis: Synthesis, Characterization and Applications.* Royal Society of Chemistry: Croydon, UK, 2018.
112. Larciprete, R.; Lacovig, P.; Gardonio, S.; Baraldi, A.; Lizzit, S. Atomic oxygen on graphite: Chemical characterization and thermal reduction. *J. Phys. Chem. C,* 2012, 116:9900-9908.
113. Yamada, Y.; Yasuda, H.; Murota, K.; Nakamura, M.; Sodesawa, T.; Sato, S. Analysis of heat-treated graphite oxide by X-ray photoelectron spectroscopy. *J. Mater. Sci.,* 2013, 48:8171-8198.
114. Alternative Asymmetric Line-Shapes. Available online: http://www.casaxps.com/

help_manual/line_shapes.htm (accessed on 1 January 2023).
115. Coates, J. *Encyclopedia of Analytical Chemistry. In Application, Theory and Instrumentation,* 2nd ed. Meyers, R.A., Ed.; Wiley: Chichester, UK, 2006; pp. 1–23.
116. Varsanyi, G. *Assignments for Vibrational Spectra of Seven Hundred Benzene Derivatives.* Hilger, A.: London, UK, 1974.
117. Baskir, E.G.; Maltsev, A.K.; Korolev, V.A.; Khabashesku, V.N.; Nefedov, O.M. Generation and IR spectroscopic study of benzyl radical. *Russ. Chem. Bull.*, 1993, 42:1438-1440.
118. Crespo-Otero, R.; Bravo-Rodriguez, K.; Roy, S.; Benighaus, T.; Thiel, W.; Sander, W.; Sánchez-García, E. Interactions of aromatic radicals with water. *Chem. Phys. Chem.,* 2013, 14:805-811.
119. Wilmshurst, J.K.; Bernstein, H.J. The infrared and Raman spectra of toluene, toluene –alfa-d4, m-xylene, and m-xylene = alfaalfa'-d6. *Can. J. Chem.*, 1957, 35:911-925.
120. Gardner, A.M.; Green, A.M.; Tamé-Reyes, V.M.; Wilton, V.H.K.; Wright, T.G. Vibrations of the low energy states of toluene (1A1 and 1B2) and the toluene cation (2B1). *J. Chem. Phys.*, 2013, 138:134303.
121. Sheka, E.; Natkaniec, I.; Rozhkova, N.; Buslaeva, E.; Tkachev, S.; Gubin, S.; Mel'Nikov, V. Parent and reduced graphene oxide of different origin in light of neutron scattering. *Nanosyst.: Phys. Chem., Math.*, 2016, 7:71-80.
122. Fillaux, F.; Papoular, R.; Lautié, A.; Tomkinson, J. Inelastic neutron-scattering study of the proton dynamics in coals. *Fuel,* 1995, 74:865-873.
123. Fuente, E.; Menndez, J.A.; Diez, M.A.; Montes-Moran, M.A. Infrared spectroscopy of carbon materials: A quantum chemical study of model compounds. *J. Phys. Chem. B,* 2003, 107:6350-6359.
124. Sheka, E.F. Digital Twins solve the mystery of Raman spectra of parental and reduced graphene oxides. *Nanomaterials*, 2022, 12:4209.
125. Singh, S.K.; Peeters, F.M. Vibrational properties of nanographene. *NanoMMTA,* 2013, 2:10-29.
126. Sheka, E.F. Virtual vibrational spectrometry of stable radicals—Necklaced graphene molecules. *Nanomaterials*, 2022, 12:597.
127. Jorio, A.; Dresselhaus, M.S.; Saito, R.; Dresselhaus, G. *Raman Spectroscopy in Graphene Related Systems.* Wiley-VCH: Weinheim, Germany, 2011.
128. Merlen, A.; Buijnsters, J.G.; Pardanaud, C. A guide to and review of the use of multiwavelength Raman spectroscopy for characterizing defective aromatic carbon solids: From graphene to amorphous carbons. *Coatings*, 2017, 7:153.
129. Tuinstra, F.; Koenig, J.L. Raman spectrum of graphite. *J. Chem. Phys.,* 1970, 53:1126.
130. Pimenta, M.A.; Dresselhaus, G.; Dresselhaus, M.S.; Cançado, L.G.; Jorio, A.; Saito, R. Studying disorder in graphite-based systems by Raman spectroscopy. *Phys. Chem. Chem. Phys.,* 2007, 9:1276-1290.
131. Venezuela, P.; Lazzeri, M.; Mauri, F. Theory of double-resonant spectra in graphene.: Intensity and line shape of defect-induced and two-phonon bands. *Phys. Rev. B.,* 2011, 84:1-25.
132. Ramos, S.L.; Pimenta, M.A.; Champi, A. Multiple-excitation study of the double-resonance Raman bands in rhombohedral graphite. *Carbon,* 2021, 179:683-691.
133. Ferrari, A.C.; Robertson, J. Raman spectroscopy of amorphous, nanostructured, diamond–like carbon, and nanodiamond. *Philos. Trans. R. Soc. A: Math. Phys. Eng. Sci.,* 2004, 362:2477-2512.
134. Mallet-Ladeira, P.; Puech, P.; Toulouse, C.; Cazayous, M.; Ratel-Ramond, N.; Weisbecker, P.; Monthioux, M. A Raman study to obtain crystallite size of carbon materials: A better alternative to the Tuinstra and Koenig law. *Carbon*, 2017, 80:629-639.
135. Mapelli, C.; Castiglioni, C.; Meroni, E.; Zerbi, G. Graphite and graphitic compounds: Vibrational spectra from oligomers to real materials. *J. Mol. Struct.*, 1999, 480-481, 615-620.
136. Mapelli, C.; Castiglioni, C.; Zerbi, G.; Müllen, K. Common force field for graphite and polycyclic aromatic hydrocarbons. *Phys. Rev. B,* 1999, 60:12710-12725.
137. Castiglioni, C.; Mapelli, C.; Negri, F.; Zerbi, G. Origin of the D line in the Raman spectrum of graphite: A study based on Raman frequencies and intensities of polycyclic aromatic hydrocarbon molecules. *J. Chem. Phys.,* 2001, 114:963-974.

138. Negri, F.; Castiglioni, C.; Tommasini, M.; Zerbi, G. A computational study of the Raman spectra of large polycyclic aromatic hydrocarbons: Toward molecularly defined subunits of graphite. *J. Phys. Chem. A,* 2002, 106:3306-3317.
139. Di Donato, E.; Tommasini, M.; Fustella, G.; Brambilla, L.; Castiglioni, C.; Zerbi, G.; Simpson, C.D.; Müllen, K.; Negri, F. Wavelength-dependent Raman activity of D2h symmetry polycyclic aromatic hydrocarbons in the D-band and acoustic phonon regions. *Chem. Phys.*, 2004, 301:81-93.
140. Negri, F.; di Donato, E.; Tommasini, M.; Castiglioni, C.; Zerbi, G.; Müllen, K. Resonance Raman contribution to the D band of carbon materials: Modeling defects with quantum chemistry. *J. Chem. Phys.*, 2004, 120:11889-11900.
141. Tommasini, M.; Castiglioni, C.; Zerbi, G. Raman scattering of molecular graphenes. *Phys. Chem. Chem. Phys.,* 2009, 11:10185-10194.
142. Golubev, Y.A.; Sheka, E.F. Peculiarities of the molecular character of the vibrational spectra of amorphous sp2 carbon: IR absorption and Raman scattering. *Proceedings of the 14th Intrnational Conference Carbon: Fundamental Problems of Material Science and Technology*, Moscow, Troitzk, 7-9 June 2022; pp. 59–60, (in Russ.).
143. Yang, X.; Han, D.; Fan, H.; Wang, M.; Du, M.; Wang, X. First-principles calculations of phonon behaviors in graphether: A comparative study with graphene. *Phys. Chem. Chem. Phys.*, 2020, 23:123-130.
144. Savosteenko, G.; Taskaev, S.; Avramov, P. Structure and Raman spectra of exotic carbon microcrystals from meteoritic dust of Chelyabinsk superbolide. *Nanomaterials,* 2023, 13:73.
145. Sheka, E.F. Molecular theory of graphene chemical modification. In: *Graphene Science Handbook: Mechanical and Chemical Properties*; Aliofkhazraei, M., Ali, N., Miln, W.I., Ozkan, C.S., Mitura, S., Gervasoni, J., Eds.; CRC Press: Boca Raton, FL, USA; Taylor and Francis Group: Abingdon, UK, 2016; pp. 312–338.
146. Rasheed, A.; San, O.; Kvamsdal, T. Digital twins: Values, challenges and enablers from a modeling perspective. *IEEE Access,* 2020, 8:21980-22012; https://doi.org/0.1109/ACCESS.2020.2970143.
147. Belousova, I.M.; Videnichev, D.A.; Kislyakov, I.M.; Krisko, T.K.; Rozhkova, N.N.; Rozhkov, S.S. Comparative studies of optical limiting in fullerene and shungite nanocarbon aqueous dispersions. *Opt. Mat. Expr.*, 2015, 5:169-175.
148. Skrypnik, L.; Babich, O.; Sukhikh, S.; Shishko, O.; Ivanova, S.; Mozhei, O.; Kochish, I.; Nikonov, I. A Study of the Antioxidant, Cytotoxic Activity and Adsorption Properties of Karelian Shungite by Physicochemical Methods. *Antioxidants,* 2021, 10:1121.
149. Sheka, E.F.; Popova, N.A.; Popova, V.A. Virtual spectrometer for sp2 carbon clusters. 1. Polycyclic benzenoid-fused hydrocarbons. *FNCN,* 2021, 29:703-715.
150. Bloino, J. A VPT2 route to near-infrared spectroscopy: The role of mechanical and electrical anharmonicity. *J. Phys. Chem. A,* 2015, 119:5269-5287.
151. Dewar, M.J.S.; Ford, G.P.; McKee, M.-L.; Rzepa, H.S.; Thiel, W.; Yamaguchi, Y. Semiempirical calculations of molecular vibrational frequencies: The MNDO method. *J. Mol. Struct.,* 1978, 43:135-138.
152. Dolganov, V.K.; Kroo, N.; Rosta, L.; Sheka, E.F.; Szabort, J. Multimode polymorphism of solid MBBA. *Mol. Cryst. Liq. Cryst.*, 1985, 127:187-194.
153. Sharma, N.; Sharma, V.; Jain, Y.; Kumari, M.; Gupta, R.; Sharma, S.K.; Sachdev, K. Synthesis and characterization of graphene oxide (GO) and reduced graphene oxide (rGO) for gas sensing application. *Macromol. Symp.,* 2017, 376:1700006.